Data driven topology optimization of AM parts accounting for process-affected fatigue performance: Application to automotive and aerospace components

International Journal of Fatigue 206 (2026) 109481

Contents lists available at ScienceDirect

International Journal of Fatigue

journal homepage: www.elsevier.com/locate/ijfatigue

Data driven topology optimization of AM parts accounting for process-affected fatigue performance: Application to automotive and aerospace components☆

Alessio Centola [a,*], Alberto Ciampaglia [a], Carlo Boursier Niutta [a], Filippo Berto [b], Davide Salvatore Paolino [a], Andrea Tridello [a]

[a] Politecnico di Torino, Department of Mechanical and Aerospace Engineering, Torino 10129, Italy
[b] Department of Chemical Engineering, Materials and Environment, Università La Sapienza, 00185 Roma, Italy

ARTICLE INFO

Keywords:
Machine learning
Topology optimization
Fatigue
Additive manufacturing
Defects
Lightweight design
Fracture Mechanics

ABSTRACT

The present paper presents two novel data-driven topology optimization (TO) procedures to design lighter additively manufactured (AM) fatigue resistant components. The first TO method is driven by a probabilistic machine learning (ML) algorithm based on a Bayesian Neural Network (BNN), trained on fatigue data from the literature to assess probabilistic stress-life (PSN) curves. These curves are used to predict the allowable design stress for TO and are predicted directly from AM process parameters, the risk volume, and thermal and surface treatments. The second TO design procedure is instead driven by another BNN, trained to predict the maximum critical defect size from the process parameters. The TO limit stress is computed from the predicted critical defect and the threshold stress intensity factor K_{th}. After the TO, the critical stress intensity factor K_I in the component is computed and compared against K_{th}, to assess the effectiveness of this design procedure. These two frameworks are applied to the design of an SS316L automotive suspension lower control arm and a Ti6Al4V aerospace bracket, respectively. With the following framework, the limit stress calculation does not require specifically designed experimental campaigns and prototyping, as previously sparse experimental knowledge can be embedded in a powerful design tool, which allows for preventing fatigue failures, while accounting directly for the influence of the AM process parameters.

Abbreviations: a_c, Critical defect size [μm]; AM, Additive Manufacturing; BNN, Bayesian Neural Network; $C(\rho)$, Global compliance of the part; C90, Confidence level at 90%; *dt_Ann*, Annealing time [hours]; *dt_HIP*, Hot Isostatic Pressing time [hours]; $\underline{F}$, External forces vector; *Fac*, Cumulative probability of a critical defect [%]; FE, Finite Element; *h*, Hatch Distance [μm]; HCF, High Cycle Fatigue; HIP, Hot Isostatic Pressing Thermal Treatment; $\underline{K(\rho)}$, Stiffness matrix; K_I, Stress Intensity Factor opening mode I [MPa•√m]; K_{th}, Threshold Stress Intensity Factor [MPa•√m]; *m*, Total mass of the part; ML, Machine Learning; m_{lim}, Upper limit mass constraint; N_f, Number of cycles to failure on the R50 PSN curve; $N_{f,R90C90}$, Number of cycles to failure on the R90C90 PSN curve; NN, Neural Network; *P*, Laser Power [W]; P_HIP, Hot Isostatic Pressing Pressure [bar]; PBF-LB, Powder Bed Fusion – Laser Beam; PS, Powder Size [μm]; PSN, Probabilistic Stress-Life (Curves); R90, Reliability level at 90%; ReLU, Rectified Linear Unit activation function; S_a, Stress amplitude [MPa]; $S_{a,R90C90}$, Stress amplitude retrieved on the R90C90 curve [MPa]; $S_{I,\max}$, 1st maximum principal stress from FE analysis [MPa]; SIF, Stress Intensity Factor; S_{lim}, Upper limit stress constraint [MPa]; SN, Stress-life curves; SS316L, Stainless Steel 316L; *ST_DN*, Deep Nitriding surface treatment Boolean; *ST_EDM*, Electric Discharge Machining Surface Treatment Boolean; *ST_EP*, Electro-polishing surface treatment Boolean; *ST_Grind*, Grinding surface treatment Boolean; *ST_LSP*, Laser Shot Peening Surface Treatment Boolean; *ST_Mac*, Machining surface treatment Boolean; *ST_Nitr*, Nitriding surface treatment Boolean; *ST_Pol*, Polishing surface treatment Boolean; *ST_SB*, Sand Blasting Surface Treatment Boolean; *ST_SMAT*, Surface Mechanical Attrition Surface Treatment Boolean; *ST_SP*, Shot Peening Surface Treatment Boolean; *ST_SSP*, Severe Shot Peening surface treatment Boolean; *ST_VF*, Vibratory Finishing surface treatment Boolean; *t*, Layer Thickness [μm]; *T_Ann*, Annealing Temperature [°C]; *T_HIP*, Hot Isostatic Pressing Temperature [°C]; TO, Topology Optimization; *TT_Ann*, Annealing (Stress relief) thermal treatment Boolean; *TT_HIP*, Hot isostatic pressing thermal treatment Boolean; $\underline{u}$, Displacement vector; *v*, Laser Scan Speed [mm/s]; V_{risk}, Risk Volume; *Y*, Reduced parameter for the Gumbel distribution; $\underline{\rho}$, Vector of design density variables; ϑ, Building Orientation [°]; ρ*, Density threshold value.

☆ This article is part of a special issue entitled: 'FDMD 5' published in International Journal of Fatigue.

* Corresponding author.
E-mail address: alessio.centola@polito.it (A. Centola).

https://doi.org/10.1016/j.ijfatigue.2026.109481
Received 25 August 2025; Received in revised form 2 January 2026; Accepted 3 January 2026
Available online 7 January 2026

1. Introduction

Additive manufacturing (AM) has rapidly advanced and is now widely adopted in sectors such as aerospace, automotive, and biomedical engineering [1–3] due to its ability to fabricate complex and lightweight geometries [4–6], such as lattices, cellular and chiral structures, unachievable with conventional manufacturing methods [7–9]. Among AM techniques, Powder Bed Fusion – Laser Beam (PBF-LB) stands out for its capability to process high-performance metal alloys, including Ti6Al4V and SS316L, with great resolution and geometric accuracy.

Despite its advantages, PBF-LB is known to introduce process-induced defects such as lack-of-fusion, porosities, gas-entrapped voids, and rough surfaces, which critically affect fatigue performance [10–12]. Various strategies have been proposed to mitigate these defects, including optimization of process parameters [13] and post-processing treatments aimed at improving surface roughness, relieving residual stresses, or lowering porosity levels [14,15]. Nonetheless, even optimized and treated components typically retain a statistically significant defect population, which reduces fatigue performance compared to conventionally manufactured counterparts [16].

The application of machine learning (ML) to predict the fatigue behavior of materials is a young research field [17,18], and AM has opened new possibilities in the matter. In fact, the effect of process parameters on both defect formation [10,16,19–21] and fatigue behavior can be captured and predicted using ML methods, to model the relationship between manufacturing conditions and structural performance. Among all ML algorithms, neural networks (NN) stand up as the most flexible, precise and scalable [22,23]. They span from purely data-driven NN to physics-informed ones [23–28], which enclose prior scientific knowledge and available experimental data at the same time [29], showing a remarkable improvement in the prediction of fatigue life [23,30–35]. However, to improve the trustworthiness and reliability of such algorithms, it is preferable to have a probabilistic formulation of the ML model, such as in [36,37] and in [35], where a probabilistic NN, namely a Bayesian NN (BNN) [38], has been created to separate the experimental uncertainty from the ML model uncertainty. Such ML framework allows to output fatigue curves that are shifted down thanks to the Owen's method [39] for improved safety.

The flexibility and design freedom of AM can be leveraged by techniques such as topology optimization (TO), which allows to reduce the component mass, without compromising its structural safety and load bearing capacity, as the part stiffness is maximized without exceeding a proper stress limit. The latter one is usually obtained with statistical methodologies and lengthy experimental campaigns, which are representative of the AM machine with a specific set of process parameters. At this preliminary TO stage, defects are not considered. For example, the influence of manufacturing defects on the fatigue performance can be verified with computed tomography (CT) scans after the production of the TOed part [40,41], with the risk that it does not meet the safety requirements and the required safety margin, depending on the application.

To address these numerous issues in TO, several attempts have been made over the years [42]. In [6], a defect-driven TO for fatigue design is proposed, where the first principal stress is reduced according to the defect distribution derived from the AM process. In [43], two TO methodologies to design against fatigue failures for AM parts have been proposed: the first one is defect driven, whereas the second one considers the size-effect while accounting for the stress distribution in the material. In [44], an aerospace bracket was optimized and manufactured by considering fatigue constraints to avoid stress concentration in critical areas. In [45], the design problems of stress constrained topology optimization with free form design domain have been addressed by proposing new computing procedures. However, to the best of the authors' knowledge, no research employs ML as a direct tool to consider at once all the influencing factors when predicting a reliable stress limit for the TO of AMed parts.

In the present paper, two components, respectively an automotive suspension lower control arm (lower control arm) made of SS316L, and an aerospace bracket made of Ti6Al4V, are designed using TO, by setting a ML-derived stress constraint. For the lower control arm, the stress constraint corresponds to the stress amplitude (S_a) at two million cycles, with 90 % confidence and 90 % reliability (R90C90), namely $S_{a,R90C90}$, predicted by the Fatigue BNN of [35]. Moreover, for the Ti6Al4V component, an alternative approach has been developed and validated, with the TO carried out by computing the limit stress from the most critical stress intensity factor (SIF) and from the critical defect size. The latter one is estimated with a BNN, which predicts the defect size starting from the process parameters. Two combinations of process parameters are considered to assess the stress limit and to run both optimizations.

The article is structured as follows: Section 2 describes the two BNNs, which predict the stress limit and the critical defect size starting from the process parameters, and the TO design procedures. Section 3 describes two case studies, the training databases employed and the results of the TO procedures. Section 4 compares the two TO procedures on the bracket and analyses the SIF validation procedure. Section 5 discusses the strengths and the limitations of this framework. Lastly, conclusions are drawn in Section 6.

2. Methods

This section describes the adopted algorithms. Section 2.1 provides details on the Fatigue BNN used to predict the stress limit with a given combination of process parameters. Section 2.2 explains the architecture of the BNN used to predict the most critical defect size a_c (Defects BNN in the following). Section 2.3 and 2.4 describe their implementation into the TO algorithm used to design components against fatigue failures.

2.1. Fatigue BNN

The Fatigue BNN is employed to predict the design stress limit against fatigue failures for the TO. The BNN has an architecture very similar to the one described in [35], enabling the calculation of the stress limit with user defined confidence and reliability levels. The BNN inherently accounts for process-affected defect distributions, which implicitly affect the resulting fatigue performances. It features an input layer, three hidden deterministic layers and an output variational layer. The number of input nodes depends on the selected alloy, as the type and number of surface treatments reported in the literature datasets varies. An input node belongs to one of these five categories: process parameters, risk volume (V_{risk}), thermal treatments, surface treatments, and stress amplitude. These input types are either reported in numeric or Boolean format. The process parameters include: building orientation ϑ [°], laser power P [W], laser scan speed v [mm/s], hatch distance h [μm], and layer thickness t [μm]. The risk volume V_{risk} [mm^3] is defined as described in [32], i.e., the volume of material that is bearing a level of stress above 90 % of the nominal stress. Thermal treatments features are divided into Boolean – for both annealing (*TT_Ann*) and hot isostatic pressing (*TT_HIP*) – and numeric – to highlight the treatment characteristics such as temperature in [°C] (*T_Ann* and *T_HIP*), duration in [hours] (*dt_HIP* and *dt_Ann*) and pressure in [bar] (*P_HIP*). As anticipated before, the surface treatments depend on the considered alloy; however, common treatments as machining (*ST_Mac*), polishing (*ST_Pol*), sand blasting (*ST_SB*), and shot peening (*ST_SP*) are common to every alloy. The last input node is referred to the equivalent stress amplitude S_a [log_{10}(MPa)] defined using the Smith-Watson-Topper correction ($S_{a,R=-1} = S_{max} \bullet \sqrt{0.5 \bullet (1-R)}$). These input nodes are connected to a pyramidal architecture of hidden layers with 100, 75 and 50 neurons, respectively, all featuring a rectified linear unit (ReLU) activation function, which shows superior performance as opposed to the other types of activation functions for the fatigue life prediction of AMed parts.

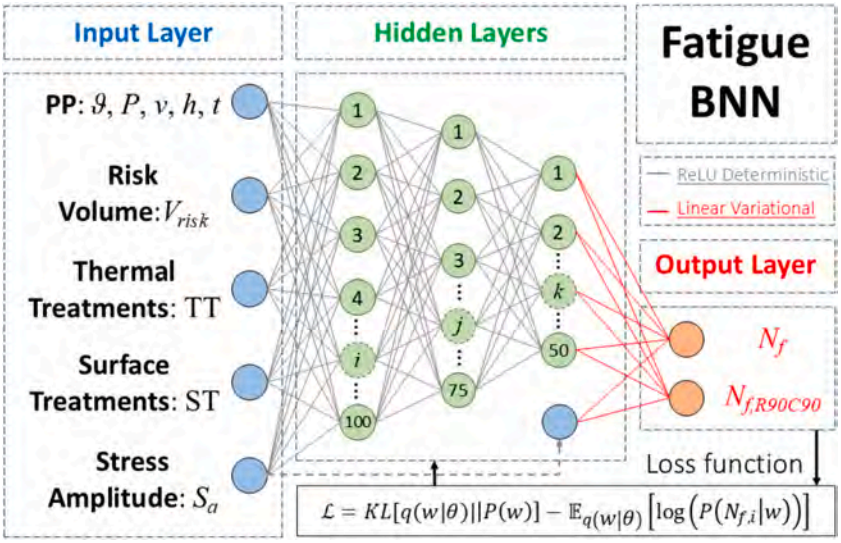

Fig. 1. Fatigue BNN structure. In blue the input nodes, in green the hidden ones and in orange the output ones. In grey deterministic ReLU connections, while in red, variational connections for the output layer. A BNN is trained by minimizing the loss function L, which includes the Kullback-Leibler [38] divergence of the learned weight distribution and the negative log likelihood of the weights [35].

This type of structure has proven to be suitable for predicting the fatigue life of PBF-LBed parts [22–24,35,46]. Since S_a influences N_f significantly more than the other inputs, the third layer has been concatenated to the input node of S_a to give it a higher importance, and to establish the correct linear relation between S_a and N_f. The hidden structure is then connected to the linearly activated variational output layer, which provides the final prediction of the training labels, namely the R50 (N_f) and R90C90 ($N_{f,R90C90}$) fatigue life. The structure of the Fatigue BNN is shown in Fig. 1. For more details about the implementation of variational layers and the BNN, the reader is referred to [35,38]. The Fatigue BNNs are trained for 1500 epochs, with a learning rate of 0.001 and a variable batch size with a training and test split of 90 %–10 %. The choice of this training split was validated for each BNN with a 10-fold cross validation, which showed comparable training and validation losses across the different folds. Moreover, the Fatigue BNN exhibits good training behavior and a very low generalization error for both materials. Additional analyses regarding the 10-fold cross validation and the Fatigue BNNs structure sensitivity analysis with considerations on the activation functions, number of layers and neurons and generalization error are available online as supplementary materials.

2.2. Defects BNN

The Defects BNN has an architecture similar to the Fatigue BNN, except for the number of inputs and the type of outputs. The training data for Ti6Al4V is the same used in [24], while the architecture has been reformulated in a probabilistic ML framework as in [35]. The inputs are the process parameters (ϑ, P, v, h and t), the mean powder size (PS) and the reduced variable $Y = -\log(-\log(Fa_c))$, calculated from the cumulative probability of a defect Fa_c. The output is the critical defect size a_c, defined as the square root area of a defect projected on a plane perpendicular to the direction of the principal stress. The inputs are

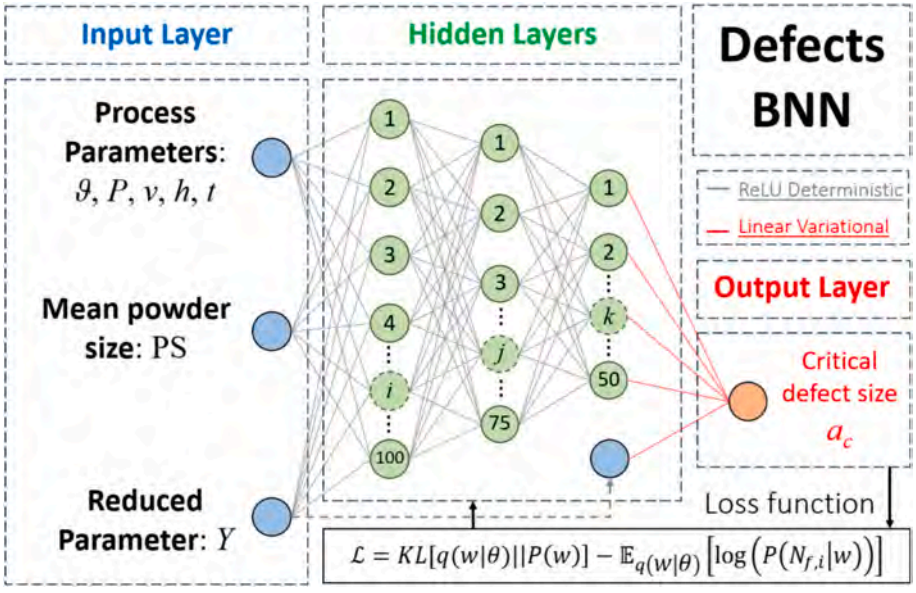

Fig. 2. Defects BNN structure: Input nodes are shown in blue, hidden neurons in green, and output nodes in orange. Deterministic ReLU connections are depicted in grey, while variational connections for the output layer are colored in red.

passed to a deterministic pyramidal structure similar to the one shown in Section 2.1, with three layers featuring 100, 75 and 50 neurons, respectively, concatenated on the third layer with the Y input. The last hidden layer is then connected to a linear variational output layer of a_c. The architecture of the Defects BNN is schematized in Fig. 2. The hyperparameters are: 1500 epochs, a learning rate of 0.001 and 15 steps per epoch, with a 90 %–10 % training-test split, which was once again validated with a 10-fold cross validation, leading to a low generalization error and a stable training process. The training database is detailed in Table 2 of Section 3.2.1. Also here, the employment of a BNN favors model improvement and a better generalization [38]. Further discussions regarding the k-fold cross validation and the Defects BNN structure (activation functions, number of layers and neurons) with overfitting analyses are available online as supplementary materials.

2.3. Topology optimization combined with the fatigue BNN

To design components against fatigue failures using TO algorithms, the commercial software Altair Hypermesh has been used. Once the material has been chosen and the BNN has been trained, the next step consists of selecting the process parameter settings that could be potentially used for the AM of the parts. In this study, the BNN is used to predict the R90C90 PSN curve, given the parameters ϑ, P, v, h, and t. Different levels of reliability and confidence can be used to train the model, depending on the application [35]. For the estimation of the PSN curves, V_{risk} is conservatively considered equal to the maximum volume available in the training database, and the material is considered as-built, i.e., without thermal and surface treatments. The TO is performed with linear elastic Finite Element (FE) analyses, using an implicit solver, as formulated in Eq. (1).

$$\begin{aligned} &\rho^* = \text{argmin } C\left(\underline{\rho}\right) \\ &\frac{m}{m_{lim}} - 1 \leq 0 \\ &\frac{S_{I,max}}{S_{lim}} - 1 \leq 0 \\ &\text{governed by } \underline{\underline{K}}\left(\underline{\rho}\right)\underline{u} = \underline{F}. \end{aligned} \tag{1}$$

In Eq. (1), $C(\underline{\rho})$ is the global compliance of the part (i.e. the function to

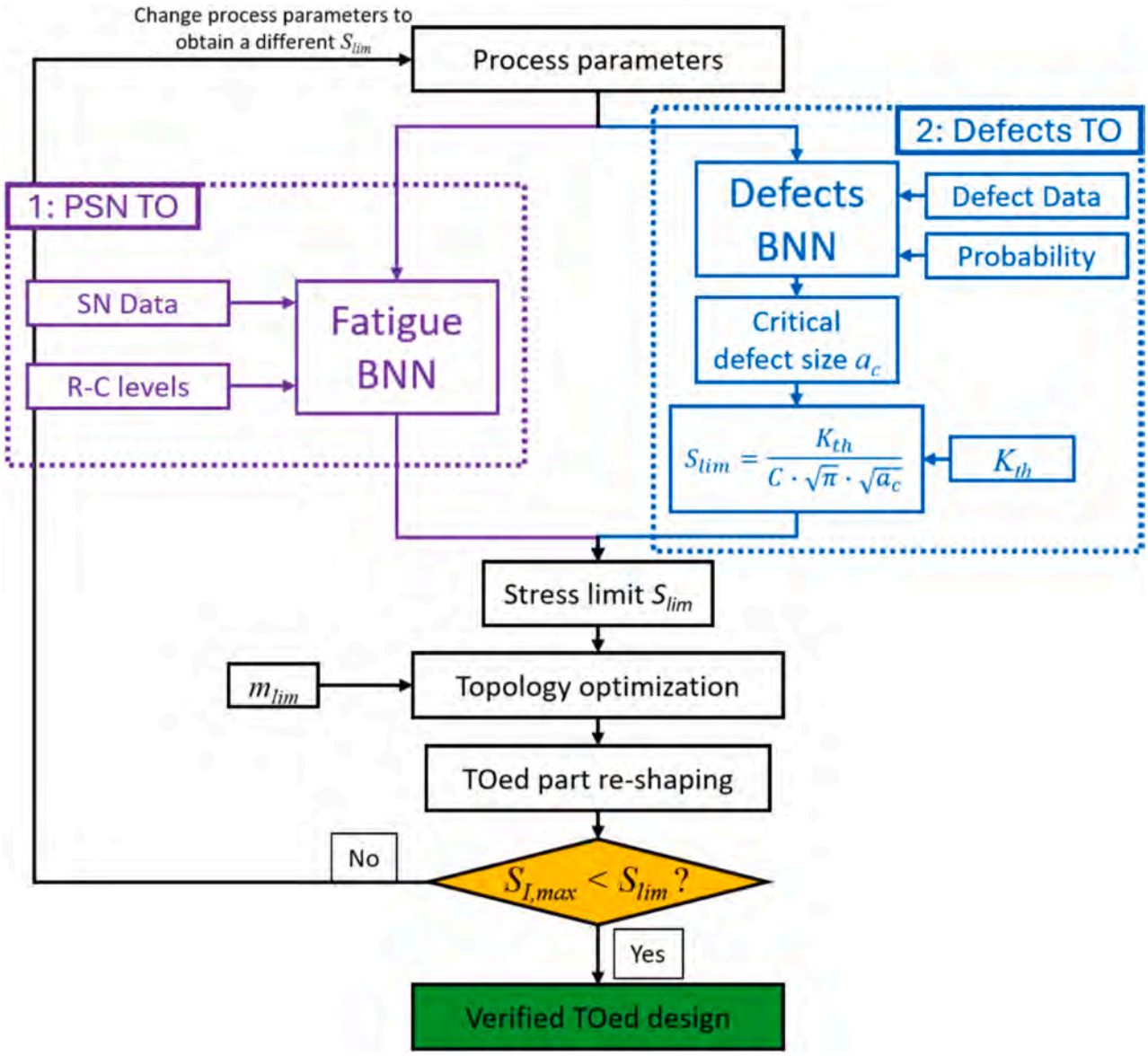

Fig. 3. Flowchart to design fatigue resistant TOed parts that account for process-affected fatigue performances. In purple, the procedure that calculates S_{lim} from the Fatigue BNN, in blue, the one that starts from the Defects BNN.

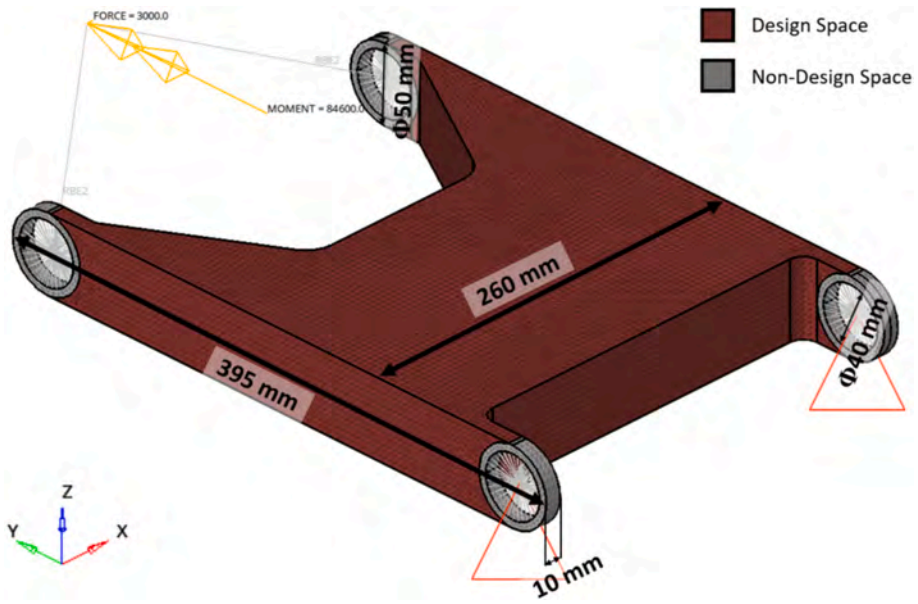

Fig. 4. SS316L automotive lower control arm initial design space, with constraints and loads.

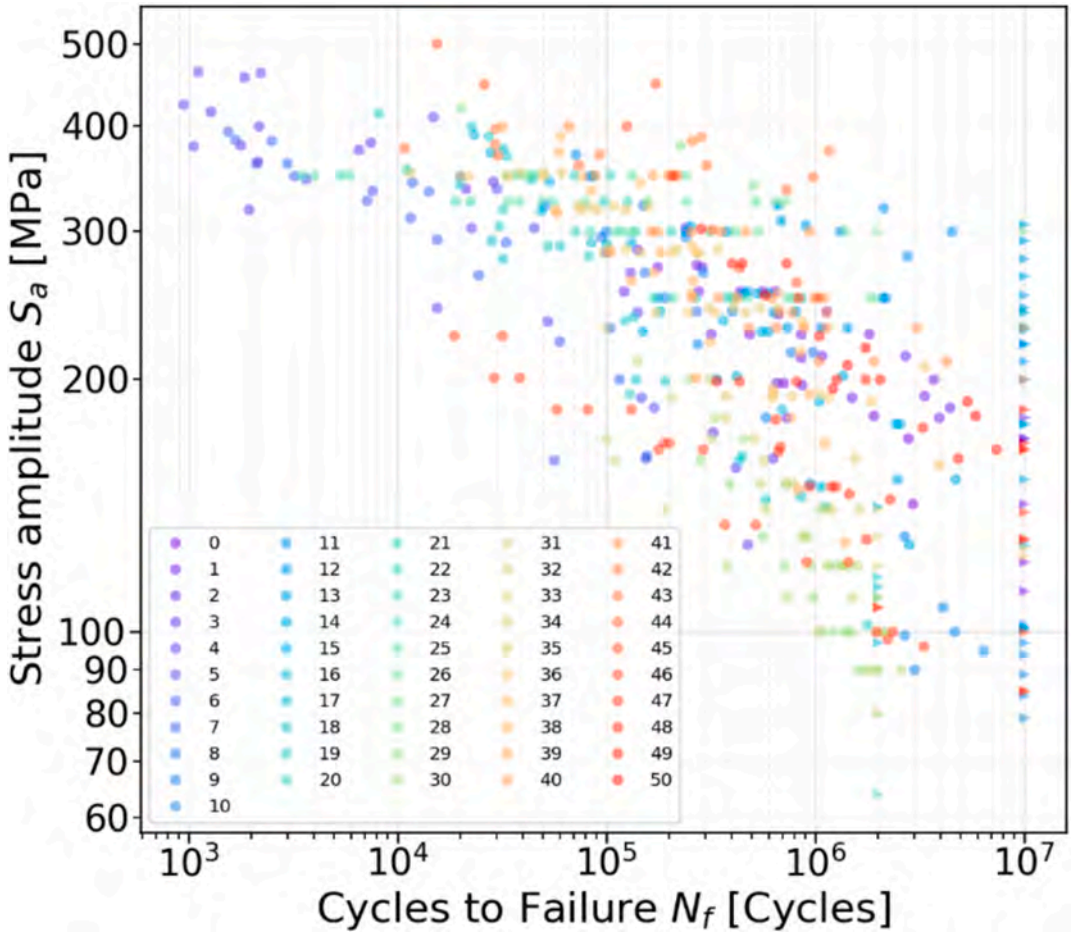

Fig. 5. All 518 SS316L training points belonging to the automotive suspension lower control arm Fatigue BNN training database, divided by dataset (refer to Table A.1 for dataset codes), displayed in the bi-logarithmic SN plane. Circular markers are failed specimens, whereas triangular ones are runouts.

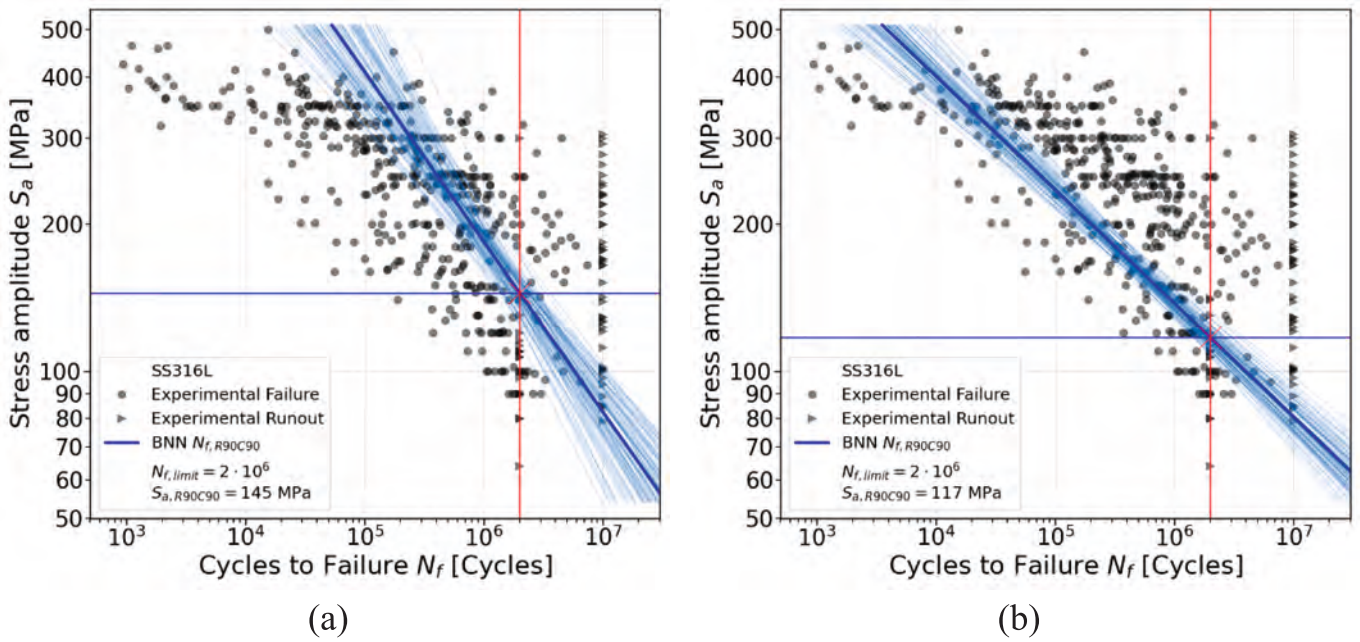

Fig. 6. Design PSN curves for the SS316L automotive suspension lower control arm, for the best (a) and worst (b) configuration of process parameters. The black points are all the instances of the training database. In red, the lifecycle limit in the HCF regimen, while in blue the R90C90 PSN curve from which the stress limit has been retrieved.

Table 1
Sets of process parameters and V_{risk} used to retrieve the corresponding design stress limit S_{lim}, from the Fatigue BNN for the SS316L automotive suspension lower control arm.

Condition	ϑ [°]	P [W]	v [mm/s]	h [μm]	t [μm]	V_{risk} [mm^3]	S_{lim} [Mpa]
Best	90	100	1200	60	20	1005	145
Worst	90	225	800	100	50	1005	117

minimize), and $\underline{\rho} = \{\rho_1, \rho_2, \ldots, \rho_N\}$ is the vector of the design variables, namely the densities of the N elements. The minimization of $C(\underline{\rho})$ must proceed without violating the upper constraints on the mass m_{lim} and stress S_{lim}, which are imposed a priori. In Eq. (1), m is the total mass of the part and $S_{I,\max}$ the maximum principal stress. S_{lim} is equal to $S_{a,R90C90}$, i.e. the limit stress calculated with the R90C90 curve obtained with the Fatigue BNN. The imposed TO stress constraint value is probabilistic in the sense that, even if the mean value is selected, the BNN is trained on R90C90 fatigue data. This specific training formulation takes into account three important sources of uncertainties, namely the epistemic and aleatoric uncertainty of fatigue (accounted by the R90C90 life) and the ML model uncertainty (accounted by the BNN) [35]. As such, the BNN allows to extract the stress constraint limit S_{lim} for the TO, both as the mean value or as the 10th percentile of the design R90C90 curve. In the following study S_{lim} is chosen as the mean value.

The results of the TO are a density map with values ranging from ρ_{inf} (equal to $10^{-5} \div 10^{-4}$, to avoid numerical instabilities) and 1. The final material distribution is then defined using a density threshold value ρ^*, by deleting all the elements with $\rho < \rho^*$. Then the geometry is reconstructed and the component is re-meshed, to check that the mass and stress constraints have not been violated. If one of the constraints is violated, a different value of ρ^* can be chosen. Once an acceptable design is identified, the geometry is re-shaped into a manufacturable AM part using the Polynurbs function of Altair Inspire, which smooths spiky areas that can create stress concentrations. Finally, the stress constraint

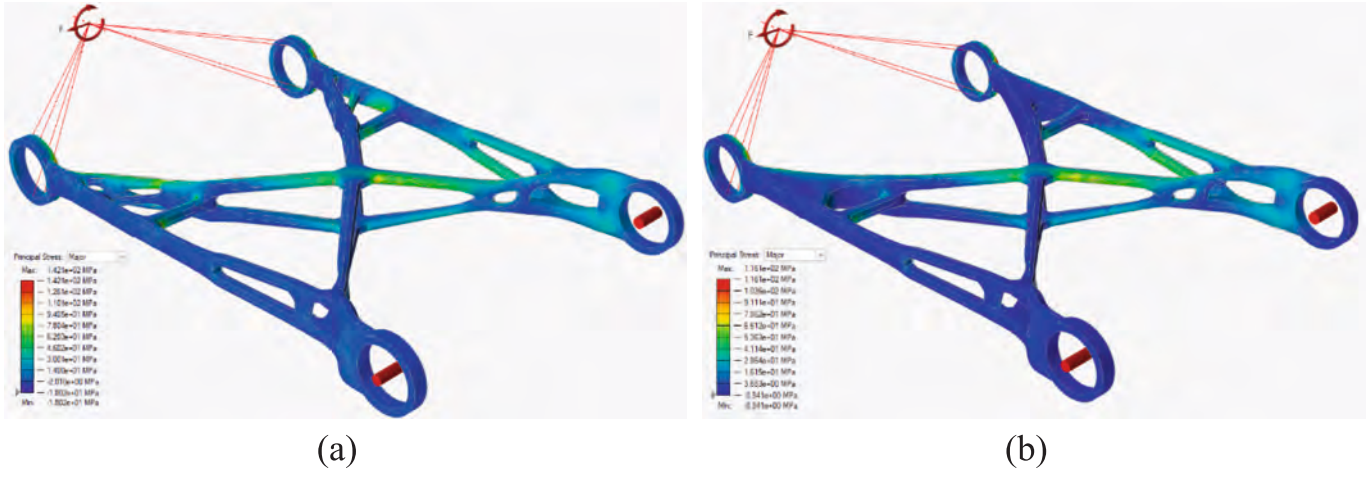

Fig. 7. FEA of the re-shaped TO geometries of the SS316L lower control arm for the best (a) and worst (b) with the S_I distribution.

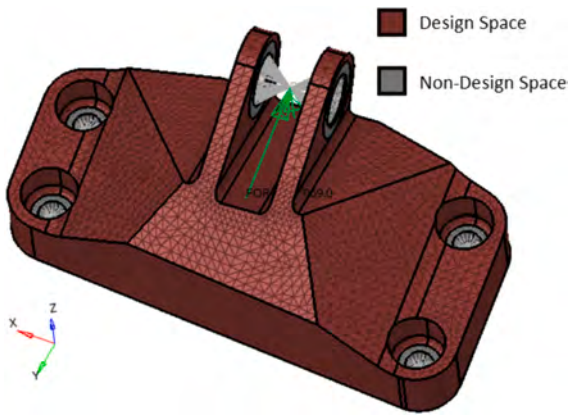

Fig. 8. Ti6Al4V aerospace bracket initial design space, with constraints and loads.

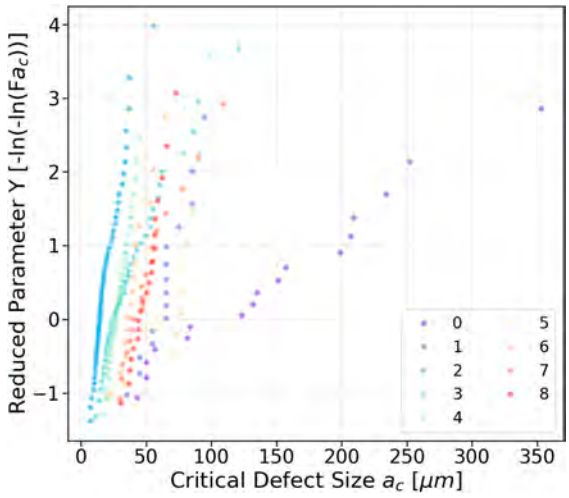

Fig. 9. All the 222 training points belonging to the defects training database of the Ti6Al4V aerospace bracket divided by dataset (refer to Table 2 for dataset code), displayed in the Gumbel plot.

is verified on the optimized geometry with a FEA. For a graphical interpretation of the procedure, the reader is referred to Fig. 3, following the purple path.

2.4. Topology optimization combined with the Defects BNN

The limit stress can be computed from the allowable SIF K_{th} using the prediction of the Defects BNN. This second approach involves a TO formulation and procedure similar to that reported in Eq. (1), but S_{lim} is calculated as in Eq. (2):

$$S_{lim} = \frac{K_{th}}{C \bullet \sqrt{\pi} \bullet \sqrt{a_c}}, \tag{2}$$

The allowable SIF K_{th} can be found in the literature or experimentally, while a_c is obtained from the Defects BNN with the investigated sets of process parameters. The corrective factor C is conservatively assumed to be equal to 0.65 (corresponding to surface defects, as opposed to 0.5 for internal defects). Once the TO is performed, the procedure follows the same steps described in Section 2.3. For a graphical interpretation of this procedure, the reader is referred to Fig. 3, considering the blue path.

3. Application to aerospace and automotive components

In this Section, the design procedures against fatigue failures are applied to two case studies: the optimization of an automotive suspension lower control arm made of SS316L using the Fatigue BNN (Section 3.1), and the optimization of an aerospace bracket made of Ti6Al4V using the Defects BNN (Section 3.2).

3.1. Automotive suspension lower control arm

The automotive lower control arm [47] is originally made of SS316L, with a total mass of 2.55 kg. For the TO, the initial design space has been defined as shown in Fig. 4. The part is connected to the application point of the loads through rigid elements, as described in [47]. A load of 3000 N along the negative x direction, and a torque of 84.6 Nm around the y direction are applied to the lower control arm, representative of a braking maneuver. As shown in Fig. 4, the design space corresponds to the region in dark red, whereas the non-design space corresponds to the grey regions. The masses of the design and non-design spaces are respectively 21.84 kg and 0.22 kg. The lower control arm has been meshed with solid tetra elements, with a mesh size of 4 mm, which yields to 169,671 elements. The following mesh size proves to be fine enough to guarantee high precision of the FE model, without leading to unnecessarily long computation times, as finer mesh sizes do not introduce significant benefits. Details regarding the mesh sensitivity analysis of the lower control arm are available as supplementary materials.

3.1.1. Training database

The process parameters and datasets collected in the SS316L training database are reported in Table A.1 of Appendix A. For the SS316L alloy, the ranges of the process parameters are the following: P ranges from 90 W to 350 W, v from 425 mm/s to 2400 mm/s, h from 60 μm to 150 μm and t from 20 μm to 50 μm. The database also reports V_{risk} to account for the size effect, which ranges from 27 mm^3 to 1005 mm^3. The thermal treatments are either annealing or HIP and are encoded with Boolean features (*TT_Ann* and *TT_HIP*), while their details are noted with numeric features. The treatment details are: the temperature (*T_Ann* and *T_HIP*), its duration (*dt_Ann* and *dt_HIP*) – which is 0 if the thermal treatment is

Table 2
Training database used to train the Defects BNN used to retrieve the critical defect size a_c for the K_{th} TO validation of the Ti6Al4V aerospace bracket.

Indexing				Process parameters					Powder size
Reference	Article	Dataset	N° Instances	Orientation ϑ [°]	Laser Power P [W]	Scan Speed v [mm/s]	Hatch Distance h [μm]	Layer Thickness t [μm]	Powder Size [μm]
[49]	1	0	17	90	175	710	120	30	41.5
[50]	2	1	15	90	280	1200	140	30	38
[51]	3	2	53	0	175	775	120	30	43
	3	3	39	45	175	775	120	30	43
	3	4	35	90	175	775	120	30	43
[52]	4	5	9	90	400	150	120	60	38.18
[53]	5	6	15	90	280	1200	140	30	45
	5	7	18	90	280	1200	140	30	34
[54]	6	8	21	90	300	1400	140	30	38

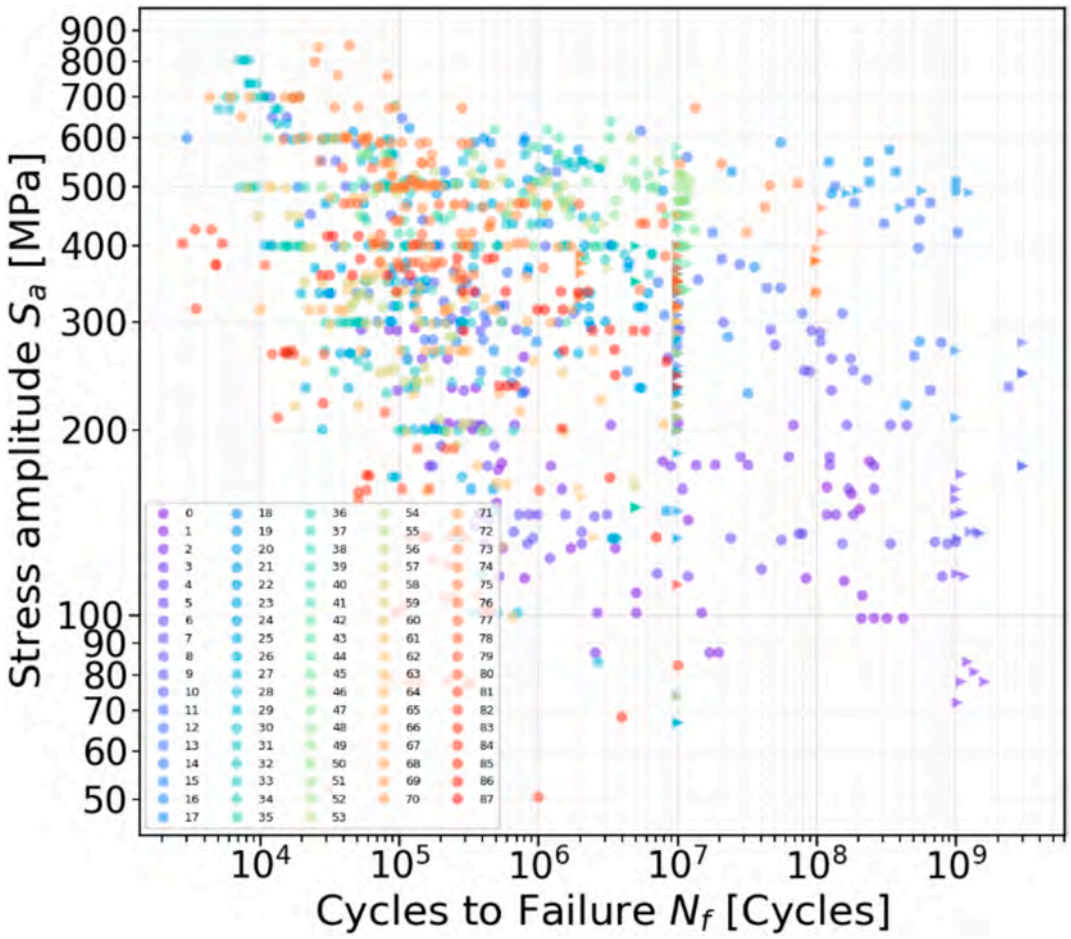

Fig. 10. All the 1106 Ti6Al4V training points belonging to the aerospace bracket training database divided by dataset (refer to Table B.1 for dataset code), displayed in the bi-logarithmic SN plane. Circular markers are failed specimens, whereas triangular ones are runouts.

Table 3
Literature K_{th} values used for the Defects BNN design procedure. To find the Slim the lowest one.

Code	$K_{th,1}$	$K_{th,2}$	$K_{th,3}$	$K_{th,4}$	$K_{th,5}$	$K_{th,6}$	$K_{th,7}$	$K_{th,8}$	$K_{th,9}$
Ref	[56]	[55]	[57]	[54]	[58]	[59]	[60]	[61]	[62]
K_{th} [MPa•√m]	2.7	4.3	5	5.5	5.63	6.5	7.234	7.5	7.8

not applied – and its pressure (*P_HIP*). Surface treatments are noted as Boolean features, and for SS316L are seven: machining (*ST_Mac*), polishing (*ST_Pol*), grinding (*ST_Grind*), vibratory finishing (*ST_VF*), nitriding (*ST_Nitr*), deep nitriding (*ST_DN*) and electro polishing (*ST_EP*). For SS316L, there are 518 training instances in total, coming from 51 experimental datasets, which come from 17 literature papers. Fig. 5 reports all the experimental datasets of the training database.

3.1.2. Topology optimization from the fatigue BNN

As anticipated in Section 2.3, the TO aims at minimizing the material usage of the part, while guaranteeing safety against fatigue loads. This workflow is ML-aided to properly define S_{lim}, which is retrieved from the Fatigue BNN with a defined set of process parameters, allowing the designer to gain control and knowledge over their influence. In TO algorithms, the portion of material not useful to bear the load is removed from the design space according to Eq. (1), by minimizing the compliance, while respecting m_{lim} and S_{lim}. This last one is retrieved from the R90C90 PSN curves (Fig. 6a-b) as $S_{a,R90C90}$, by interrogating the Fatigue BNN with two sets of process parameters: one leading to a higher S_{lim}, and one yielding a lower one, which will be referred to as the best and the worst case throughout the article, to simplify the discussion. This has been done to assess the limits of this procedure. The required fatigue life for the lower control arm is $N_f = 2 \bullet 10^6$ cycles, which has been used to calculate the required fatigue limit S_{lim} from the predicted PSN curve.

V_{risk} has been set to the largest value in the database (1005 mm^3) to have a conservative estimate. No thermal or surface treatments have been considered. The two process parameter cases are reported in Table 1 and will be referred to as the "best" and "worst" conditions throughout the paper.

Once the stress limits are defined, the TO is run for both cases achieving convergence in less than 100 iterations. For the best one, an S_{lim} of 145 MPa has been imposed, whereas for the worst case, an S_{lim} of 117 MPa has been considered. Once the TO has successfully converged, the geometry is reconstructed, with a mass of 1.98 kg and 2.32 kg (22.4 % and 9.1 % mass reduction with respect to the original component), for the best and worst cases. Fig. 7a-b shows the stress distribution for the optimized components. Both designs are verified, with a $S_{I,\max}$ of 142.1 and 116.1 MPa for the best and worst case, respectively. Additional analyses of the TO convergence of the lower control arm are reported as supplementary material.

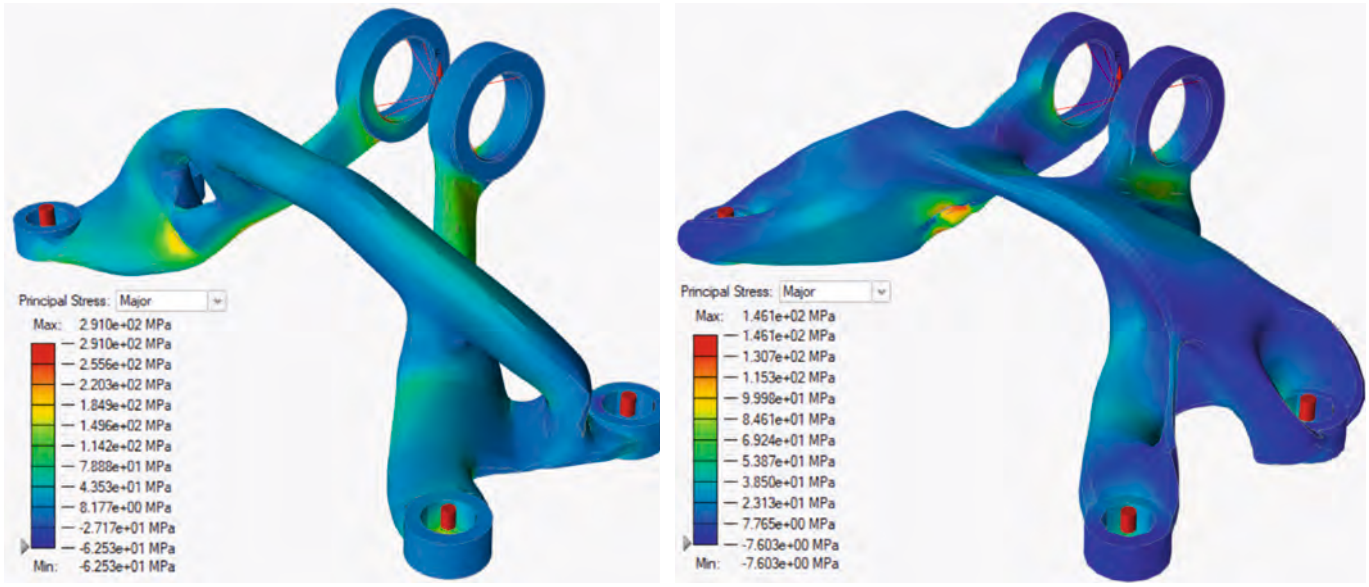

Fig. 11. FE stress analysis of the re-shaped geometries for the best (a) and worst (b) case, shown with the S_I distribution, for the Ti6Al4V aerospace bracket with the inverse TO approach that starts from the Defects BNN and the Kth values.

3.2. Aerospace bracket

The aerospace bracket described in [48] is made of Ti6Al4V, with an initial weight of 2.06 kg (Fig. 8). The bracket is constrained at the four bottom holes and is subjected to a load of 10560 N, with an angle of 40° with respect to the negative *y*-axis. The load has been applied to the midpoint of the two top holes using rigid element connectors. The mass of the non-design space (grey) is 0.19 kg, while the mass of the design space (dark red) is 1.87 kg. The bottom holes have an inner diameter of 10 mm and an outer diameter of 16 mm, with a depth of 8 mm, whereas the two top holes are 6.5 mm deep and have an inner diameter of 20 mm and an outer one of 29 mm. The bracket was meshed with solid tetrahedral elements with a size of 4 mm again, resulting in 119,288 elements. This mesh resolution is sufficient to achieve high accuracy in the FE model and avoids excessive computation time, since additional refinement does not significantly enhance the results. A mesh sensitivity analysis of the bracket has also been reported as supplementary material.

3.2.1. Training database

The database used for the Defects BNN TO of the bracket contains the defect distributions obtained using different parameters for the AM of Ti6Al4V. 222 training points (Fig. 9) have been collected from six literature papers, resulting in nine training datasets. As for the Fatigue BNN, the process parameters such as ϑ, P, v, h, t and the powder size, have been labelled in the defects training database (Table 2).

The Ti6Al4V Fatigue BNN training database is similar to the SS316L one. However, the surface treatments for the Ti6Al4V are: *ST_Mac*, *ST_Pol*, *ST_Grind*, sand blasting (*ST_SB*), shot peening (*ST_SP*), laser shot peening (*ST_LSP*), surface mechanical attrition (*ST_SMAT*) and electric discharge machining (*ST_EDM*). As reported in Table B.1, there are 1106 training points from 88 experimental datasets, retrieved from 32 articles. The process parameters ranges are the following: P goes from 95 W to 450 W, v from 150 mm/s to 1900 mm/s, h from 50 μm to 180 μm and t from 20 μm to 60 μm. As can be observed in Fig. 10, the order of magnitude of N_f ranges from 10^3 to 10^9 while S_a ranges from 50 MPa to 850 MPa. This training database is used to derive S_{lim} to drive the TO for the Ti6Al4V aerospace bracket, so that both fatigue and defect driven TO can be directly compared in Section 4.1.

3.2.2. Topology optimization from the defects BNN

The results of the TO based on the Defects BNN are hereby reported for the bracket, where S_{lim} is calculated as in Eq. (2). The maximum a_c is retrieved from the Defects BNN with a Fa_c of 90 %, and two sets of process parameters, yielding respectively to a high a_c (172 μm, worst case) and to a low one (137.5 μm, best case). Given the variability in dataset sizes for the Defects BNN, Fa_c = 90 % was selected as it is the highest Fa_c consistently reachable across all datasets (the smallest dataset of Table 2 contains 9 samples, allowing a maximum Fa_c of 90 %). This choice ensures that the BNN is not queried with input features beyond its training range. K_{th} is chosen as the lowest one, among the available literature K_{th} values with similar process parameters to the best and worst case. This has been done to have the most conservative scenario. Among the values reported in Table 3, the lowest K_{th} values – that are also similar in terms of process parameters to the best and worst case – are 4.3 MPa•$\sqrt{m}$ [55] and 2.7 MPa•$\sqrt{m}$ [56], respectively.

The resulting S_{lim} are 318 MPa and 179 MPa, for the best and worst case. The TOs achieve a stable convergence in less than 80 and 40 iterations for the best and worst case respectively.

The re-shaped parts have been reported in Fig. 11a-b, with results highly similar to the reconstructed TO results: a $S_{I,\max}$ of 291 MPa and a final mass of 0.28 kg (86.4 % mass reduction with respect to the original part), for the best case, and a $S_{I,\max}$ of 146.1 MPa and a final mass of 0.35 kg (83.1 % mass reduction), for the worst case. Additional details regarding the TO convergence of the bracket are available as supplementary materials.

4. Validation

Considering that the two TO procedures are highly dependent on the type and number of available data, the SS316L lower control arm can only be designed with the Fatigue BNN, given the scarcity of K_{th} values

Table 4
Summary of the TO procedure that starts from defects and literature K_{th} values, for the Ti6Al4V aerospace bracket.

	Input Features								Constraints		TO results				Re-shaping		
Condition	ϑ	P	v	h	t	PS_{mean}	Fa_c	a_c	K_{th} min		S_{lim}	m_{lim}	ρ^*	$S_{I,max}$	m	Δm	$S_{I,max}$	m	Δm
Units	[°]	[W]	[mm/s]	[μm]	[μm]	[μm]	[%]	[μm]	[MPa•√m]		[MPa]	[kg]	[%]	[MPa]	[kg]	[%]	[MPa]	[kg]	[%]
Best	90	400	750	60	35	41.28	90	137.5		4.3	318	0.3	55	308	0.26	87.4	291	0.28	86.4
Worst	90	100	1100	60	35	41.28	90	172		2.7	179	0.5	75	164	0.38	81.6	146	0.35	83.1

and defect data in the literature. Although the defect-based TO allows to explicitly account for the presence of defects, it has one major limit: it is complex to retrieve K_{th} and a_c data, both experimentally and in the literature. Obtaining experimental K_{th} values is a time-consuming procedure. On the contrary, S-N fatigue data are more readily available, making the fatigue-based TO more favorable from a data availability perspective. Despite this, it is still necessary to verify if the fatigue BNN can correctly account for the presence of defects. Section 4.1 compares the two methodologies applied to the bracket, since enough Ti6Al4V data is available for both fatigue curves and defect distributions. In Section 4.2 the K_{th} verification for the Ti6Al4V bracket is explained, to validate the trustworthiness and the effectiveness in implicitly considering defects of the Fatigue BNN.

4.1. Fatigue BNN based TO for the aerospace bracket

As for the lower control arm, the TO is performed for the two cases, with S_{lim} retrieved on the R90C90 PSN curves obtained from the Ti6Al4V Fatigue BNN, interrogated with the same sets of process parameters used in the Defects BNN TO (Table 4). As shown in Fig. 12a-b, S_{lim} is 224 MPa for the best, and 79 MPa for the worst case (Table 5). Once again, V_{risk} has been set to maximum value (10560 mm^3), and no thermal and surface treatments have been applied. The predictions of the Fatigue BNN are consistent with the one of the Defects BNN: a higher S_{lim} is associated to the process parameters set that produces a lower a_c (best case), and a lower S_{lim} is associated to the process parameters set that yields a higher a_c (worst case). The TO converges after 35 and 28 iterations for the best and worst case.

Fig. 13a-b shows the final re-shaped parts, with a final $S_{I,\max}$ of 208.3 MPa and a mass of 0.33 kg (84 % mass reduction), for the best case, and a $S_{I,\max}$ of 70.1 MPa and a mass of 1.01 kg (51 % mass reduction), for the worst case.

Comparing these results with the ones of the defects procedure (Section 3.2.2, Table 4), it is evident how this approach leads to a lower S_{lim} (224 MPa as opposed to 318 MPa for the best case, and 79 MPa as opposed to 179 MPa for the worst case), hence to a lower mass reduction, as shown in Table 6. From this analysis it can be deduced that these higher S_{lim} for the Defects BNN TO, may be due to the data scarcity issue highlighted before, both in terms of literature K_{th} values and a_c. On the other hand, given that there are five times more data points coming from more than 80 datasets for the Ti6Al4V Fatigue BNN, the S_{lim} estimate can be considered more representative, and this may even be the reason behind its lower value. However, both TO methods are in agreement as both S_{lim} obtained with the worst setting are pairwise smaller than their best process parameters counterparts. This analysis shows that the Fatigue BNN TO may be more preferable, given that S-N data is more easily available and that the assessment of S_{lim} is faster compared to the Defects BNN TO. However, this depends on the data available to the designer.

4.2. K_{th} validation

The geometries designed with the aid of the Fatigue BNN are safe, given that $S_{I,\max} < S_{lim}$ for all design cases. However, to verify if the Fatigue BNN provides reliable results and predictions when a defect originates the fatigue failure, the following procedure has been followed. Starting from the defect size a_c estimated with the Defects BNN, and by considering the same process parameters in input, the SIF K_I, for the most critical defect, is calculated according to Eq. (3) and are then compared with literature K_{th} values:

$$K_I = C \bullet S_{I,max} \bullet \sqrt{\pi} \bullet \sqrt{a_c}, \tag{3}$$

with $S_{I,\max}$ being the maximum 1st principal stress from the FE analysis of the aerospace bracket TOed with the Fatigue BNN and with a_c being the critical defect size obtained from the Defects BNN. This last one has been queried with the same sets of process parameters of Section 3.2.2,

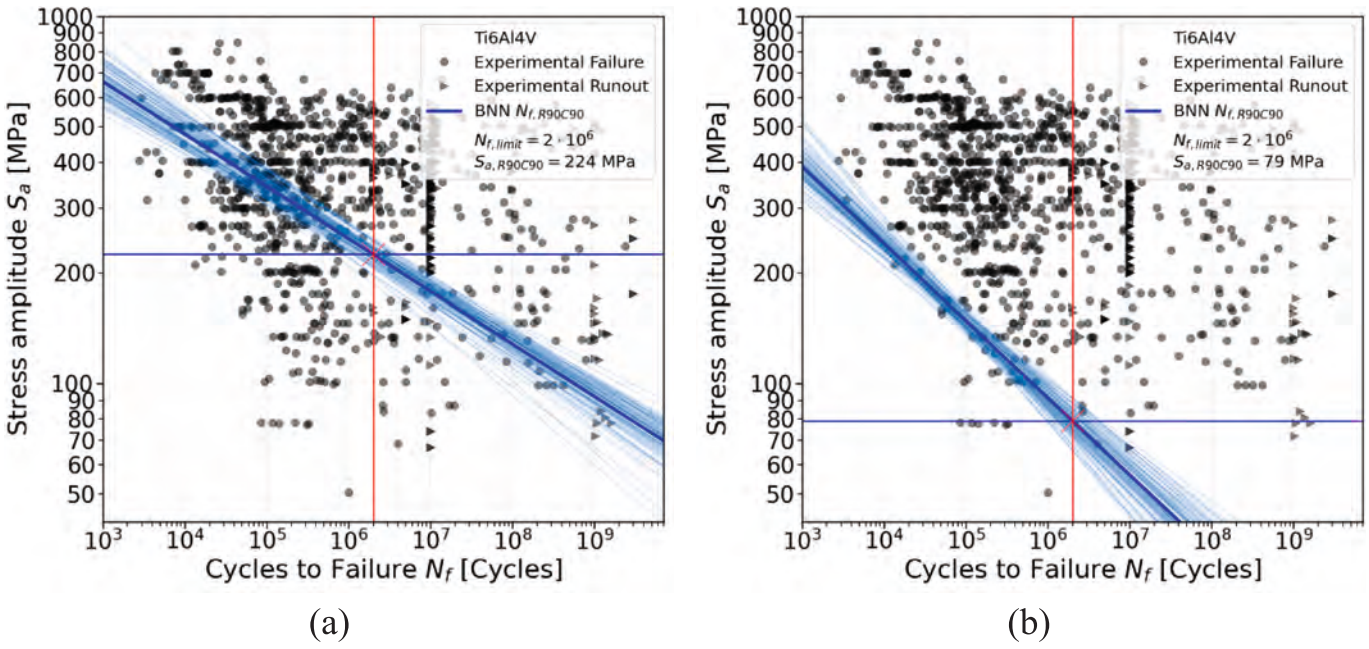

Fig. 12. Design PSN curves for the Ti6Al4V aerospace bracket, for the best (a) and worst (b) configuration of process parameters. The black points are all the instances of the training database. In red the lifecycle limit in the HCF regimen, while in blue the R90C90 from which the stress limit has been retrieved.

Table 5
Sets of process parameters used to retrieve the corresponding design S_{lim} as $S_{a,R90C90}$, from the Fatigue BNN for the Ti6Al4V aerospace bracket.

Condition	ϑ [°]	P [W]	v [mm/s]	h [μm]	t [μm]	V_{risk} [mm^3]	$S_{a,R90C90}$ [MPa]
Best	90	400	750	60	35	10,560	224
Worst	90	100	1100	60	35	10,560	79

which lead to the same values of a_c as shown in Table 7.

This yields to a K_I of 2.77 MPa•√m and 1.03 MPa•√m, for the best and worst case. These ones are then compared with the lowest literature K_{th} values with similar process parameters, namely 4.3 MPa•√m for the best and 2.7 MPa•√m for the worst case, which are the same used to derive S_{lim} for the Defects BNN TO. It can be clearly seen that both K_I are smaller than their respective K_{th}. This proves the trustworthiness of the Fatigue BNN to account for the defect influence. Indeed, the Fatigue BNN is capable of implicitly accounting for the presence of defects, as all failures used to train the Fatigue BNN originate from them.

5. Discussion

AMed components like, the lower control arm and bracket hereby used as examples, exhibit significantly different complexities and geometrical features with respect to standardized specimens found in the literature datasets used to train the Fatigue and Defects BNN. Hence, the cyclic response of these specimens may differ substantially from the

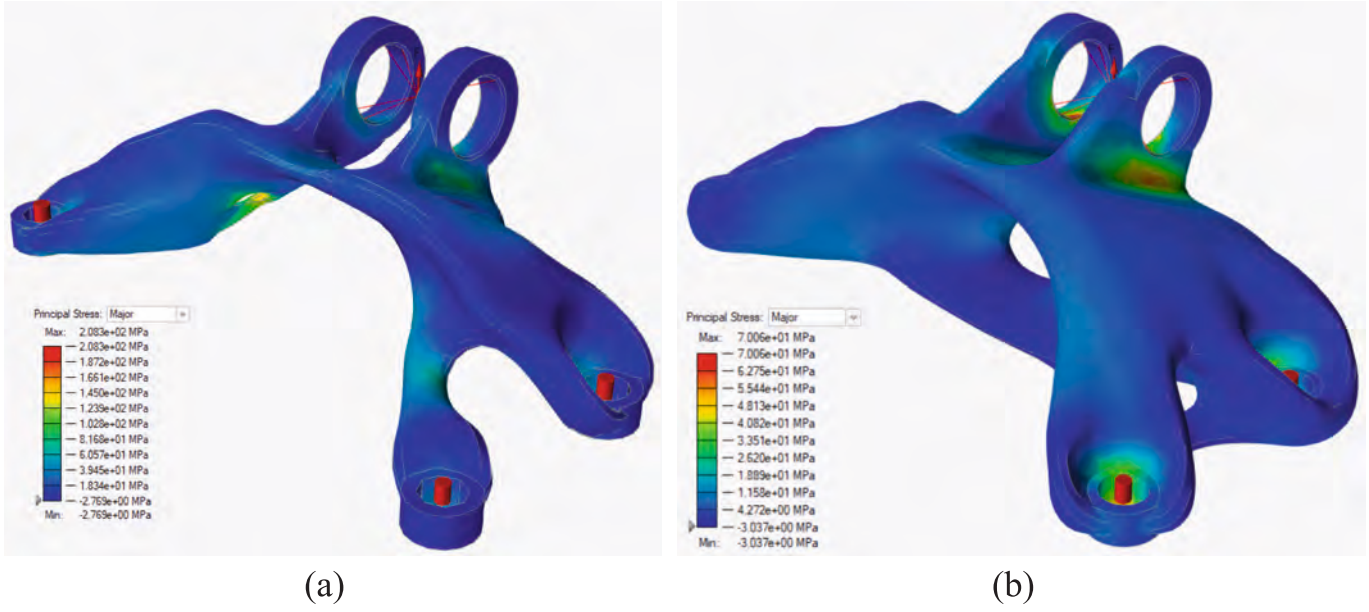

Fig. 13. FE stress analysis of the TOed Ti6Al4V aerospace bracket from the Fatigue BNN. The best (a) and worst (b) case geometries are shown re-shaped with the S_I distribution.

Table 6
Summary of both ML driven TO procedures for the Ti6Al4V aerospace bracket.

		Input parameters									Constraints		TO results			Re-shaping		
BNN	Case	ϑ	P	v	h	t	V_{risk}	PS_{mean}	Fa_c	a_c	K_{th} min	S_{lim}	m_{lim}	ρ^*	$S_{I,max}$	m	Δm	$S_{I,max}$	m	Δm
Units		[°]	[W]	[mm/s]	[μm]	[μm]	[mm^3]	[μm]	[%]	[μm]	[MPa•√m]	[MPa]	[kg]	[%]	[MPa]	[kg]	[%]	[MPa]	[kg]	[%]
Defects BNN	Best	90	400	750	60	35	–	41.28	90 %	137.5	4.3	318	0.3	55 %	308	0.26	87.4 %	291	0.28	86.4 %
	Worst	90	100	1100	60	35	–	41.28	90 %	172	2.7	179	0.5	75 %	164	0.38	81.6 %	146	0.35	83.1 %
Fatigue BNN	Best	90	400	750	60	35	10,560	–	–	–	–	224	0.5	77.5 %	205	0.35	83 %	208.3	0.33	84 %
	Worst	90	100	1100	60	35	10,560	–	–	–	–	79	1	47.5 %	68	1.04	49.5 %	70	1.01	51 %

one of actual components. Therefore, the reason behind the employment of this data-driven tool lies behind the fact that it allows to design lightweight TOed AM components in a simplified manner, while imposing S_{lim} constraint that account for the design against fatigue failures. In fact, literature data are exploited to guide the design process, while accounting for the inherent scatter of fatigue performance of materials and for the influence of process parameters. Nevertheless, given the geometrical and V_{risk} differences between specimens and components, it is important to make conservative design choices, to counteract possible limitations introduced with this simplification. For example, when designing parts the R90 curve can be chosen to extract S_{lim}. Here instead the R90C90 curve is adopted which yields more conservative results. Moreover, when querying the Fatigue BNN with the process parameters, the maximum V_{risk} is adopted and, this choice is indeed conservative, as it yields to lower fatigue performances [15], as opposed to smaller volumes (Fig. 14).

When the design procedure employs the Defects BNN, a_c is extracted with a Fa_c of 90 % instead of lower values (e.g. 50 %), and this latter one is considered to be located in the component most critical point, i.e. where $S_{I,\max}$ is applied. Additionally, when the stress limit is calculated with the Defects BNN and Eq. (2), the corrective factor C is conservatively assumed to be equal to 0.65. This choice yields to a lower stress limit value as opposed to 0.5, which refers to internal defects. If a component designed with this framework is employed in critical applications, it is obviously necessary to carry out dedicated experimental tests for validation. Nevertheless, by incorporating experimental findings reported in the literature, the statistical significance of the fatigue data and the influence of process parameters, the proposed methodologies allow to guide the design process of AM components, especially in the early design phase. Alternatively, higher reliability and confidence levels (e.g. 95 % or 99 % as opposed to 90 %) could be adopted by the designer, as the two BBNs easily allows to do so. Nonetheless, the employment of these several conservative design choices, leads to lightweight and fatigue resistant parts, which are even proven not to be overdesigned as, even in the worst process parameter case, a considerable mass reduction can be achieved. Moreover, given the ability of the Fatigue BNN to account for V_{risk}, it must be verified whether the conservative choice to consider the maximum V_{risk} for both alloys to assess the PSN curve has been respected or not in the final re-shaped geometries. To this end, the volume of the region undergoing a stress above 90 % (V_{90}) of $S_{I,\max}$ has been computed via FEA, and it corresponds to the risk-volume according to [32], for all parts TOed with the Fatigue BNN. As shown in Fig. 15, the FEA of the re-shaped parts designed from the Fatigue BNN shows only the portion of material undergoing a stress above 90 % of the $S_{I,\max}$. The resulting volumes are respectively of 88.77 mm^3 and 52.46 mm^3, for the best (Fig. 15a) and worst (Fig. 15b) case of the SS316L lower control arm, and 33.65 mm^3 and 25.83 mm^3, for the best (Fig. 15c) and worst (Fig. 15d) case of the Ti6Al4V bracket, respectively. This shows that having used and assumed the maximum V_{risk} as input has been a conservative estimate for the analyzed components, since the V_{90} are significantly smaller and within the training ranges. In fact, although the fatigue BNN has been trained only on specimens whose maximum V_{risk} are of 1005 mm^3 for the lower control arm and of 10560 mm^3 for the bracket, this analysis shows that the TOed geometries present several notched regions that lead to small V_{90}. In addition, the Fatigue BNN mirrors the actual experimental evidence [15], as to high V_{risk} correspond lower fatigue performance and vice-versa for low V_{risk}. Moreover, the V_{risk} sensitivity analysis reported in Fig. 14, shows that using the maximum V_{risk} value, not only yields a lower R90C90 life, but also a smaller degree of uncertainty, as the confidence band shrinks as V_{risk} increases. This reduced uncertainty associated to the maximum V_{risk} and its employment when querying the BNN, has limited implications that at most yield to a safer component.

It must be noted that an iterative approach which adjusts S_{lim} as a function of the V_{risk} of the component during the TO process could relax the conservative S_{lim} constraints obtained by considering the maximum

Table 7
Process parameters used to retrieve a_c from the Defects BNN, whose related K_I value has been calculated with the corresponding $S_{I,max}$ for the Ti6Al4V aerospace bracket TOed with the Fatigue BNN.

Condition	ϑ	P	v	h	t	PSmean	Fa_c	a_c	$S_{I,max}$	K_I	K_{th}
	[°]	[W]	[mm/s]	[μm]	[μm]	[μm]	%	[μm]	[MPa]	[MPa•√m]	[MPa•√m]
Best	90	400	750	60	35	41.28	90	137.5	205	2.77	4.3
Worst	90	100	1100	60	35	41.28	90	172	68	1.03	2.7

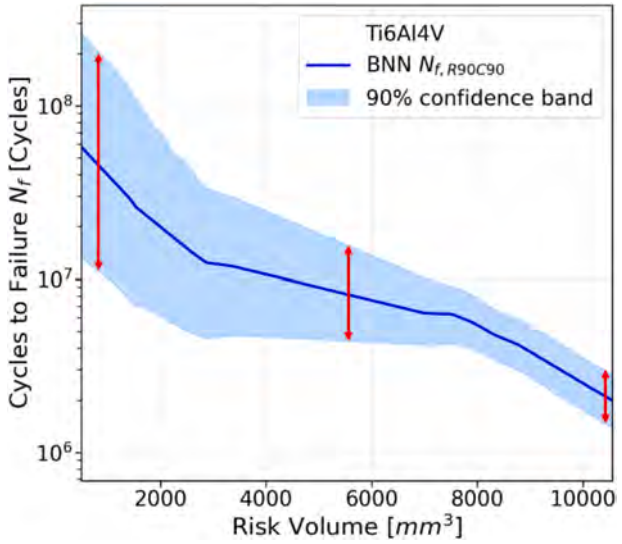

Fig. 14. Sensitivity study of V_{risk} on the R90C90 fatigue life for the Ti6Al4V bracket. The BNN allows to output both the mean value (blue) as well as the 90 % confidence band (light blue) of the predicted R90C90 fatigue life, which shrinks as V_{risk} increases. This shows that to the maximum V_{risk} value not only is associated a lower life, but also a smaller degree of uncertainty.

V_{risk}. However, this would complicate the TO process and significantly increase its duration. Therefore, the designs obtained with the maximum V_{risk} can be considered safe and easy to implement. However, it is important to note that this applies to these specific components and must be verified case by case, i.e., the risk-volume considered in the ML algorithm should be equal or above the risk-volume of the component after the TO.

It should also be pointed out that, with respect to previous research activities [23,35], several novel aspects have been introduced in the present work. The Fatigue BNN is not only trained on SS316L, but also on Ti6Al4V to predict S_{lim} for the bracket. Previously a deterministic Defect FFNN was proposed [24], whereas here the Defects BNN is novel, as it has been declined probabilistically, allowing to determine the critical defect size a_c, to later compute S_{lim} starting also from literature K_{th} values. Additionally, the a_c output from the Defects BNN is used to estimate K_I for the best and worst process parameters case with $S_{I,max}$ computed from the FE analysis of the parts TOed with the Fatigue BNN. These K_I values are shown to be smaller when compared to literature K_{th}, corroborating the trustworthiness of the Fatigue BNN procedure and its capabilities to implicitly account for the presence of defects, given that fatigue failures are originated by them. These two BNN model types are key integral modules of this framework, that actively affect the outcome of the design procedure of the part to be designed against fatigue failure with TO. Furthermore, the trustworthiness of the procedure can be assessed by using both BNNs simultaneously to design the same component, provided that there is enough data for both BNNs as for the aerospace bracket. With this, the Fatigue BNN has shown to be more conservative, as it estimates a lower S_{lim} with respect to the Defects BNN. Beyond that, the Fatigue BNN driven TO may also be preferable from a data availability point of view, given that fatigue failures data is more readily available as opposed to critical defects data. Additionally, coherence holds between the two BNNs, as the best process parameter set leads to the highest S_{lim} and the smallest a_c, and the worst process parameters set leads to the smallest S_{lim} and the highest a_c. To the best of the authors' knowledge, this is the first paper to present simultaneously two data driven design approaches to compute the TO S_{lim} against fatigue failures: a direct process to fatigue performances approach (from process to life: Fatigue BNN), and a process to crack propagation root cause approach (from process to defects: Defects BNN). Ultimately, with these considerations and the conservative design choices listed at the beginning of this section, the following data driven TO framework allows to design lightweight AMed components, making additional intermediate part production for the defects assessment and further prototyping optional.

6. Conclusions

The present work presents an approach for the design against fatigue failures of metallic components, whose geometry is optimized with topology optimization (TO) algorithms, to be produced by means of Additive Manufacturing (AM) processes. In particular, the stress limit (S_{lim}) to be considered in the TO process is estimated by using Machine Learning (ML) algorithms, which receive as input the process parameters set during the manufacturing process. The procedure has been applied to an automotive suspension lower control arm and an aerospace bracket, respectively made of SS316L and Ti6Al4V. The following final remarks summarize the key aspects of the present work:

- For each material, a Bayesian neural network (BNN) is trained on fatigue failures literature data of the respective alloy, using data for Ti6Al4V and for SS316L. This Fatigue BNN is used to retrieve the corresponding design probabilistic stress-life (PSN) curve, from which the design S_{lim} for the TO is computed.
- Two different designs have been obtained for each component: one with a set of process parameters that leads to a higher S_{lim}, the other with a process parameters combination that yields a lower S_{lim}.
- The proposed ML framework allows the S_{lim} assessment by exploiting literature data into a single design tool, that accounts for the inherent scatter of fatigue performance of materials and for the influence of process parameters, thus allowing for the reliable fatigue design of AM components through TO.
- A Defects BNN has been trained to compute the maximum critical defect size a_c from the process parameters, from which the most critical stress intensity factor K_I for the optimized component can be computed. The estimated K_I is compared with threshold values K_{th} retrieved from the literature. The outcome of this comparison verifies the trustworthiness of the design procedures, as K_I (2.77 and 1.03 MPa•√m, for the best and worst case) is lower than the lowest K_{th} (4.3 and 2.7 MPa•√m).
- These results also confirm that the Fatigue BNN is capable of implicitly accounting for the presence of defects, as this BNN is trained on fatigue failures that originate from defects.
- Another TO procedure has also been proposed for the Ti6Al4V aerospace bracket. Its S_{lim} has been computed from literature K_{th} values and the critical defect sizes, derived from the Defects BNN. This defect driven TO leads to a higher S_{lim} with respect to the Fatigue BNN TO for the Ti6Al4V aerospace bracket.

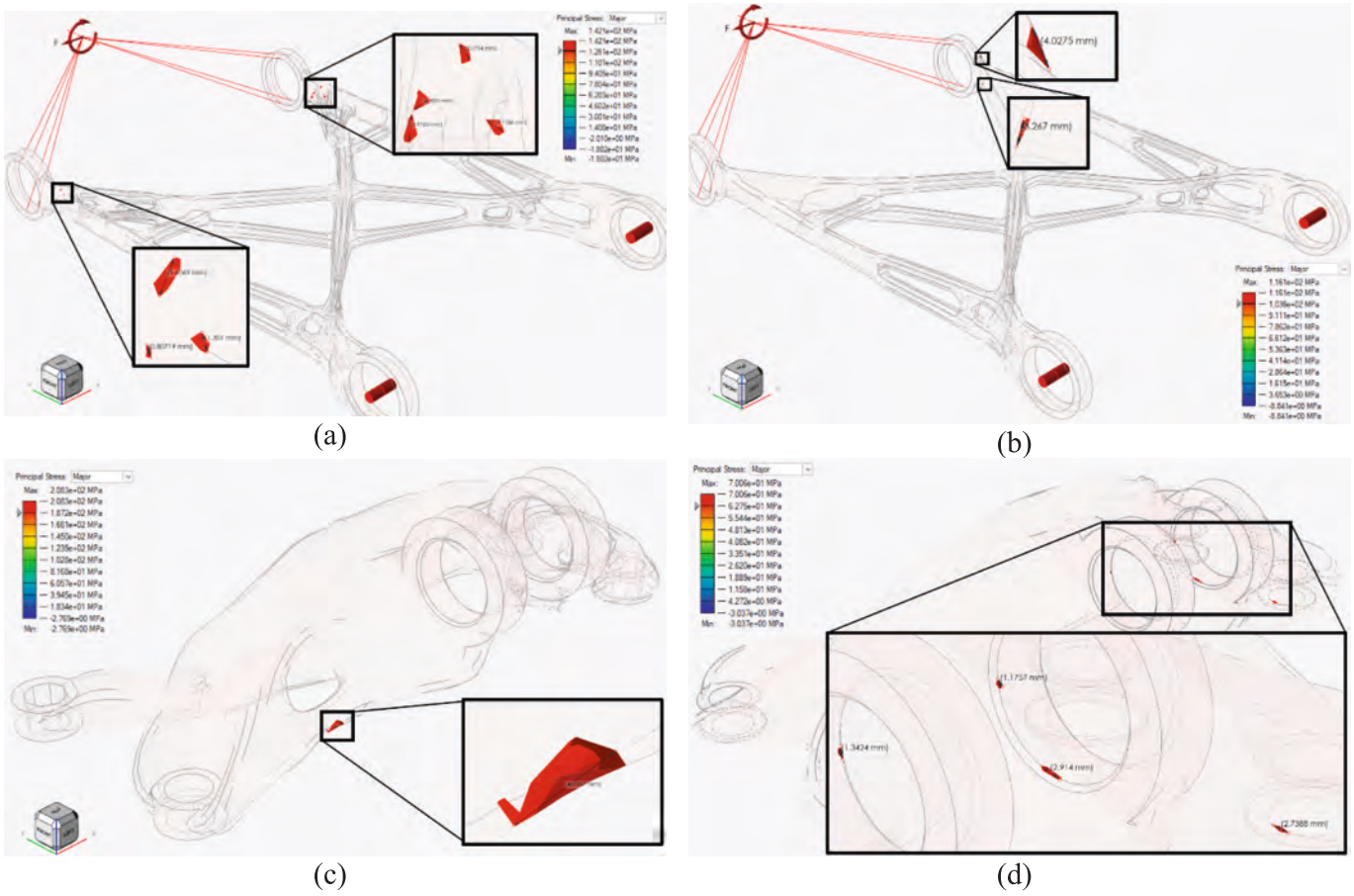

Fig. 15. V_{90} analysis on the re-shaped geometries TOed with the Fatigue BNN. The portions of material highlighted in red are undergoing 90 % of $S_{I,max}$. The resulting V_{90} are respectively of 88.77 mm^3, 52.46 mm^3, 33.65 mm^3 and 25.83 mm^3, for the best (a) and worst (b) case of the SS316L lower control arm and for the best (c) and worst (d) case of the Ti6Al4V aerospace bracket.

- With this architecture designers can reliably calculate the limit stress against fatigue failures, without specifically designed experiments and by avoiding intermediate part production, as previously neglected and scattered experimental data can be leveraged to train a single design tool, that accounts for the process-induced fatigue performances.

In conclusion, the proposed design methodologies can be used to lighten AM parts with a data-driven TO, which allows for embedding the influence of process parameters, thermal treatments, surface treatments and manufacturing defects during the design stage and not after the component production. Moreover, the developed ML algorithms allow avoiding long and expensive experimental campaigns, as it is possible to obtain S_{lim} while inferring the process influence, by leveraging the experimental data and previous knowledge available in the literature.

CRediT authorship contribution statement

Alessio Centola: Writing – original draft, Visualization, Methodology, Investigation, Data curation, Conceptualization. **Alberto Ciampaglia:** Writing – review & editing, Validation, Supervision, Conceptualization. **Carlo Boursier Niutta:** Writing – review & editing, Validation, Supervision, Conceptualization. **Filippo Berto:** Writing – review & editing, Supervision. **Davide Salvatore Paolino:** Writing – review & editing, Supervision, Project administration, Conceptualization. **Andrea Tridello:** Writing – review & editing, Supervision, Project administration, Formal analysis, Conceptualization.

Funding

This research did not receive any specific grant from funding agencies in the public, commercial, or not-for-profit sectors.

Declaration of competing interest

The authors declare that they have no known competing financial interests or personal relationships that could have appeared to influence the work reported in this paper.

Appendix A

SS316L fatigue BNN training database

Table A.1
. Training database used to train the Fatigue BNN used to retrieve the stress limit for the TO design of the SS316L automotive suspension lower control arm.

Indexing				Process Parameters					Risk Volume	Thermal Traetments							Surface Treatments						
Reference	Article	Dataset	N° Specimens	Orientation ϑ [°]	Laser Power P [W]	Scan Speed v [mm/s]	Hatch Distance h [μm]	Layer Thickness t [μm]	Risk Volume V_{risk} [mm^3]	TT_Ann	T_Ann	dt_Ann	TT_HIP	T_HIP	P_HIP	dt_HIP	ST_Mac	ST_Pol	ST_Grind	ST_VF	ST_Nitr	ST_DN	ST_EP
[63]	1	0	7	90	103	425	130	30	28.90	0	20	0	0	20	1	0	0	0	0	0	0	0	0
	1	1	14	90	103	425	130	30	28.90	0	20	0	0	20	1	0	1	0	0	0	0	0	0
	1	2	16	90	103	425	130	30	28.90	0	20	0	0	20	1	0	1	1	0	0	0	0	0
[64]	2	3	10	0	350	1000	100	30	173.18	0	20	0	0	20	1	0	1	1	0	0	0	0	0
	2	4	10	90	350	1000	100	30	173.18	0	20	0	0	20	1	0	1	1	0	0	0	0	0
	2	5	10	45	350	1000	100	30	173.18	0	20	0	0	20	1	0	1	1	0	0	0	0	0
	2	6	10	90	350	1000	100	30	173.18	0	20	0	0	20	1	0	0	0	0	0	0	0	0
	2	7	10	45	350	1000	100	30	173.18	0	20	0	0	20	1	0	0	0	0	0	0	0	0
[65]	3	8	6	0	250	800	100	50	81.29	0	20	0	0	20	1	0	1	1	0	0	1	0	0
	3	9	6	0	250	800	100	50	81.29	0	20	0	0	20	1	0	1	1	0	0	0	1	0
[66]	4	10	18	90	190	750	120	30	603.30	0	20	0	0	20	1	0	0	1	0	0	0	0	0
	4	11	11	90	190	750	120	30	603.30	0	20	0	0	20	1	0	1	1	0	0	0	0	0
	4	12	10	90	190	750	120	30	603.30	1	900	2	0	20	1	0	0	1	0	0	0	0	0
	4	13	13	90	190	750	120	30	603.30	1	900	2	0	20	1	0	1	1	0	0	0	0	0
[67]	5	14	19	90	90	1000	150	30	86.39	1	500	1	0	20	1	0	0	1	0	0	0	0	0
[68]	6	15	6	0	175	750	100	30	27.00	0	20	0	0	20	1	0	0	0	1	0	0	0	0
	6	16	6	0	175	550	100	50	27.00	0	20	0	0	20	1	0	0	0	1	0	0	0	0
	6	17	7	45	175	750	100	30	27.00	0	20	0	0	20	1	0	0	0	1	0	0	0	0
	6	18	8	45	175	550	100	50	27.00	0	20	0	0	20	1	0	0	0	1	0	0	0	0
	6	19	10	90	175	750	100	30	27.00	0	20	0	0	20	1	0	0	0	1	0	0	0	0
	6	20	8	90	175	550	100	50	27.00	0	20	0	0	20	1	0	0	0	1	0	0	0	0
[69]	7	21	7	90	200	1000	110	50	661.87	1	1038	1	0	20	1	0	0	0	0	0	0	0	0
	7	22	8	90	200	1000	110	50	172.45	1	1038	1	0	20	1	0	0	0	0	0	0	0	0
	7	23	8	90	195	1083	90	20	661.87	1	1038	1	0	20	1	0	0	0	0	0	0	0	0
	7	24	8	90	195	1083	90	20	172.45	1	1038	1	0	20	1	0	0	0	0	0	0	0	0
	7	25	8	90	200	1000	110	50	661.87	1	1038	1	0	20	1	0	1	1	0	0	0	0	0
	7	26	7	90	200	1000	110	50	172.45	1	1038	1	0	20	1	0	1	1	0	0	0	0	0
	7	27	5	90	195	1083	90	20	172.45	1	1038	1	0	20	1	0	1	1	0	0	0	0	0
[70]	8	28	4	0	195	1083	90	20	272.93	0	20	0	0	20	1	0	1	1	0	0	0	0	0
[71]	9	29	12	90	275	700	100	50	1005.31	1	620	1.5	0	20	1	0	0	0	0	0	0	0	0
	9	30	12	90	275	700	100	50	1005.31	1	620	1.5	0	20	1	0	0	1	0	0	0	0	0
	9	31	15	90	275	700	100	50	60.00	1	620	1.5	0	20	1	0	0	0	0	0	0	0	0
	9	32	15	90	275	700	100	50	60.00	1	620	1.5	0	20	1	0	0	1	0	0	0	0	0
	9	33	11	90	275	700	100	50	60.00	1	620	1.5	0	20	1	0	0	1	0	0	0	0	0
[72]	10	34	22	90	245	960	100	30	346.84	0	20	0	1	900	1000	2	0	1	0	0	0	0	0
	10	35	21	90	245	960	100	30	346.84	0	20	0	0	20	1	0	0	1	0	0	0	0	0
[73]	11	36	7	0	250	1083	90	20	45.89	0	20	0	0	20	1	0	0	0	0	0	0	0	0
	11	37	8	90	250	1083	90	20	45.89	0	20	0	0	20	1	0	0	0	0	0	0	0	0
	11	38	5	0	250	1083	90	40	45.89	0	20	0	0	20	1	0	0	0	0	0	0	0	0
	11	39	6	90	250	1083	90	40	45.89	0	20	0	0	20	1	0	0	0	0	0	0	0	0
[74]	12	40	16	0	195	1083	90	20	144.00	0	20	0	0	20	1	0	0	0	0	0	0	0	1
	12	41	14	0	195	1083	90	20	144.00	0	20	0	0	20	1	0	0	0	0	0	0	0	1
[75]	13	42	4	90	195	1083	90	20	294.52	0	20	0	0	20	1	0	1	1	0	0	0	0	0
	13	43	4	90	195	1083	90	20	294.52	1	900	0.167	0	20	1	0	1	1	0	0	0	0	0
	13	44	5	90	195	1083	90	20	294.52	1	1050	0.167	0	20	1	0	1	1	0	0	0	0	0
[76]	14	45	10	0	180	1200	60	30	161.01	1	650	2	0	20	1	0	1	0	0	0	0	0	0
[21]	15	46	15	90	320	2400	100	50	190.85	0	20	0	0	20	1	0	0	0	0	0	0	0	0
[77]	16	47	10	90	275	760	120	50	171.26	0	20	0	0	20	1	0	0	0	0	0	0	0	0
	16	48	14	90	275	760	120	50	171.26	0	20	0	0	20	1	0	0	0	0	1	0	0	0
	16	49	13	90	275	760	120	50	171.26	0	20	0	0	20	1	0	1	0	0	0	0	0	0
[78]	17	50	9	90	113	600	80	20	933.05	0	20	0	0	20	1	0	1	0	0	0	0	0	0

Table B.1
. Training database used to train the Fatigue BNN used to retrieve the stress limit for the TO design of the Ti6Al4V aerospace bracket.

Indexing				Process Parameters					Risk Volume	Thermal Traetments							Surface Treatments							
Ref	Article	Dataset	N° Specimens	Orientation ϑ [°]	Laser Power P [W]	Scan Speed v [mm/s]	Hatch Distance h [μm]	Layer Thickness t [μm]	Risk Volume V_{risk} [mm^3]	TT_Ann	T_Ann	dt_Ann	TT_HIP	T_HIP	P_HIP	dt_HIP	ST_Mac	ST_Pol	ST_Grind	ST_SB	ST_SP	ST_LSP	ST_SMAT	ST_EDM
[13]	1	0	12	90	120	1200	70	30	45.89	1	600	2	0	20	1	0	0	1	0	0	0	0	0	0
	1	1	17	90	120	1000	100	45	45.89	1	600	2	0	20	1	0	0	1	0	0	0	0	0	0
	1	2	14	90	120	800	130	60	45.89	1	600	2	0	20	1	0	0	1	0	0	0	0	0	0
	1	3	16	90	160	1000	130	30	45.89	1	600	2	0	20	1	0	0	1	0	0	0	0	0	0
	1	4	17	90	160	800	70	45	45.89	1	600	2	0	20	1	0	0	1	0	0	0	0	0	0
	1	5	13	90	160	1200	100	60	45.89	1	600	2	0	20	1	0	0	1	0	0	0	0	0	0
	1	6	14	90	200	800	100	30	45.89	1	600	2	0	20	1	0	0	1	0	0	0	0	0	0
	1	7	13	90	200	1200	130	45	45.89	1	600	2	0	20	1	0	0	1	0	0	0	0	0	0
	1	8	16	90	200	1000	70	60	45.89	1	600	2	0	20	1	0	0	1	0	0	0	0	0	0
	1	9	19	90	160	1000	70	30	45.89	1	600	2	0	20	1	0	0	1	0	0	0	0	0	0
[49]	2	10	16	90	175	710	120	30	45.60	1	800	2	0	20	1	0	1	0	0	0	0	0	0	0
	2	11	19	90	175	710	120	30	50.62	1	800	2	0	20	1	0	1	1	0	0	0	0	0	0
	2	12	16	90	175	710	120	30	50.62	0	20	0	1	920	1000	2	1	1	0	0	0	0	0	0
[54]	3	13	21	90	280	1200	140	30	149.60	1	500	2	0	20	1	0	0	1	0	0	0	0	0	0
[79]	4	14	5	90	200	1000	100	50	769.69	0	20	0	0	20	1	0	1	0	0	0	0	0	0	0
	4	15	3	90	200	1000	100	50	769.69	0	20	0	1	930	1300	3	1	0	0	0	0	0	0	0
[80]	5	16	15	90	200	1250	80	30	1500.43	1	820	1.5	0	20	1	0	0	0	0	0	0	0	0	0
[81]	6	17	10	0	190	1000	65	30	59.36	1	955	2	0	20	1	0	0	1	0	0	0	0	0	0
	6	18	10	0	190	1000	65	30	59.36	0	20	0	0	20	1	0	0	1	0	0	0	1	0	0
[62]	7	19	17	90	360	1200	100	60	23.58	1	710	2	1	920	1000	2	0	1	1	0	0	0	0	0
	7	20	14	90	360	1200	100	60	7.72	1	710	2	1	920	1000	2	0	1	1	0	0	0	0	0
[82]	8	21	12	45	170	1250	100	30	149.60	1	650	3	0	20	1	0	0	0	0	0	0	0	0	0
	8	22	12	45	170	1250	100	30	149.60	1	650	3	0	20	1	0	0	1	0	0	0	0	0	0
	8	23	15	45	170	1250	100	30	149.60	1	650	3	0	20	1	0	0	0	0	0	1	0	0	0
[83]	9	24	12	90	120	960	100	30	63.62	0	20	0	0	20	1	0	1	1	0	1	0	0	0	0
	9	25	11	90	120	540	100	30	63.62	0	20	0	0	20	1	0	1	1	0	1	0	0	0	0
	9	26	11	90	120	400	100	30	63.62	0	20	0	0	20	1	0	1	1	0	1	0	0	0	0
	9	27	12	90	120	1260	100	30	63.62	0	20	0	0	20	1	0	1	1	0	1	0	0	0	0
	9	28	9	90	120	1500	100	30	63.62	0	20	0	0	20	1	0	1	1	0	1	0	0	0	0
[52]	10	29	9	90	400	150	120	60	133.78	0	20	0	0	20	1	0	1	0	0	0	0	0	0	0
	10	30	22	90	400	150	120	60	133.78	0	20	0	1	850	2000	2	1	0	0	0	0	0	0	0
[56]	11	31	20	90	170	1200	100	30	471.24	0	20	0	0	20	1	0	0	0	0	0	0	0	0	0
[84]	12	32	18	90	200	1250	80	30	149.60	0	20	0	1	920	1020	2	0	0	0	0	0	0	0	0
	12	33	20	90	200	1250	80	30	149.60	0	20	0	1	920	1020	2	1	1	0	0	0	0	0	0
	12	34	12	90	200	1250	80	30	149.60	1	820	1.5	0	20	1	0	1	1	0	0	0	0	0	0
[53]	13	35	16	90	280	1200	140	30	339.29	1	900	1	0	20	1	0	0	0	0	0	0	0	0	0
	13	36	17	90	280	1200	140	30	339.29	1	900	1	0	20	1	0	0	0	0	0	0	0	0	0
	13	37	20	90	280	1200	140	30	235.62	1	900	1	0	20	1	0	1	1	0	0	0	0	0	0

(*continued on next page*)

Table B.1 (*continued*)

Indexing				Process Parameters					Risk Volume	Thermal Traetments							Surface Treatments							
Ref	Article	Dataset	N° Specimens	Orientation ϑ [°]	Laser Power P [W]	Scan Speed v [mm/s]	Hatch Distance h [μm]	Layer Thickness t [μm]	Risk Volume V_{risk} [mm^3]	TT_Ann	T_Ann	dt_Ann	TT_HIP	T_HIP	P_HIP	dt_HIP	ST_Mac	ST_Pol	ST_Grind	ST_SB	ST_SP	ST_LSP	ST_SMAT	ST_EDM
	13	38	20	90	280	1200	140	30	235.62	1	900	1	0	20	1	0	1	1	0	0	0	0	0	0
[85]	14	39	11	90	280	1200	50	30	129.53	0	20	0	0	20	1	0	0	0	0	0	0	0	0	0
	14	40	11	90	280	1200	50	30	129.53	0	20	0	1	900	1200	2	1	0	0	0	0	0	0	0
	14	41	10	90	280	1200	50	30	129.53	0	20	0	1	900	1200	2	1	0	0	0	0	0	1	0
[86]	15	42	11	90	280	1200	140	30	21.74	0	20	0	0	20	1	0	1	1	0	0	0	0	0	0
	15	43	3	90	280	1200	140	30	21.74	1	920	0.5	0	20	1	0	1	1	0	0	0	0	0	0
	15	44	6	90	280	1200	140	30	21.74	1	920	0.5	0	20	1	0	1	0	0	0	1	0	0	0
	15	45	12	90	280	1200	140	30	21.74	0	20	0	0	20	1	0	1	1	0	0	0	0	0	0
	15	46	7	90	280	1200	140	30	21.74	1	920	0.5	0	20	1	0	1	1	0	0	0	0	0	0
	15	47	7	90	280	1200	140	30	21.74	1	920	0.5	0	20	1	0	1	0	0	0	1	0	0	0
	15	48	8	90	340	1250	120	60	21.74	0	20	0	0	20	1	0	1	1	0	0	0	0	0	0
	15	49	4	90	340	1250	120	60	21.74	1	920	0.5	0	20	1	0	1	1	0	0	0	0	0	0
	15	50	6	90	340	1250	120	60	21.74	1	920	0.5	0	20	1	0	1	0	0	0	1	0	0	0
	15	51	9	90	340	1250	120	60	21.74	0	20	0	0	20	1	0	1	1	0	0	0	0	0	0
	15	52	4	90	340	1250	120	60	21.74	1	920	0.5	0	20	1	0	1	1	0	0	0	0	0	0
	15	53	5	90	340	1250	120	60	21.74	1	920	0.5	0	20	1	0	1	0	0	0	1	0	0	0
[87]	16	54	12	90	280	1200	140	30	1200.00	1	650	3	0	20	1	0	0	0	0	0	0	0	0	0
	16	55	7	90	280	1200	140	30	1200.00	1	650	3	0	20	1	0	0	0	0	0	0	1	0	0
[88]	17	56	22	0	285	1200	140	30	63.66	1	650	3	0	20	1	0	1	0	0	0	0	0	0	0
[89]	18	57	9	90	280	1200	140	30	294.00	1	700	1	0	20	1	0	0	0	0	0	0	0	0	0
	18	58	9	90	280	1200	140	30	294.00	1	700	1	0	20	1	0	0	1	0	0	0	0	0	0
[90]	19	59	13	90	370	1250	90	60	239.46	1	650	2	0	20	1	0	0	0	0	0	0	0	0	0
	19	60	9	90	370	1250	90	60	239.46	1	650	2	0	20	1	0	1	1	0	0	0	0	0	0
[91]	20	61	7	0	220	660	90	60	577.27	0	20	0	0	20	1	0	0	0	0	0	0	0	0	0
	20	62	11	0	220	660	90	60	577.27	1	850	2	0	20	1	0	0	0	0	0	0	0	0	0
[92]	21	63	9	0	95	300	80	25	1300.00	0	20	0	0	20	1	0	0	1	0	0	0	0	0	0
[93]	22	64	19	90	125	925	80	20	107.84	1	950	0.5	0	20	1	0	1	0	0	0	0	0	0	0
[94]	23	65	27	90	170	1250	100	30	339.29	1	650	3	0	20	1	0	0	0	0	0	0	0	0	1
[59]	24	66	10	90	175	710	125	30	199.12	0	20	0	0	20	1	0	1	0	0	0	0	0	0	0
	24	67	10	0	175	710	125	30	199.12	0	20	0	0	20	1	0	1	0	0	0	0	0	0	0
[95]	25	68	8	90	300	1000	120	40	712.75	1	500	2	0	20	1	0	0	1	0	0	0	0	0	0
	25	69	6	90	300	1000	120	40	712.75	1	500	2	1	920	1000	2	0	1	0	0	0	0	0	0
	25	70	6	90	300	1000	120	40	712.75	1	920	2	0	20	1	0	0	1	0	0	0	0	0	0
	25	71	6	90	300	1000	120	40	712.75	1	550	4	0	20	1	0	0	1	0	0	0	0	0	0
[96]	26	72	17	90	450	1200	150	50	31.94	1	850	2	0	20	1	0	1	0	0	0	0	0	0	0
	26	73	20	45	450	1200	150	50	31.94	1	850	2	0	20	1	0	1	0	0	0	0	0	0	0
	26	74	22	0	450	1200	150	50	31.94	1	850	2	0	20	1	0	1	0	0	0	0	0	0	0
[60]	27	75	20	90	125	925	80	20	191.31	1	950	0.5	0	20	1	0	1	0	0	0	0	0	0	0
[97]	28	76	12	90	280	1200	50	50	129.53	1	900	2	0	20	1	0	1	0	0	0	0	0	0	0
[98]	29	77	24	0	350	1250	100	60	149.60	1	800	2	0	20	1	0	1	0	0	0	0	0	0	0
	29	78	19	0	350	1250	100	60	149.60	1	800	2	0	20	1	0	1	0	0	0	0	0	0	0
[99]	30	79	15	0	200	200	180	50	10560.00	0	20	0	0	20	1	0	1	1	0	0	0	0	0	0
	30	80	7	90	200	200	180	50	10560.00	0	20	0	0	20	1	0	1	1	0	0	0	0	0	0
	30	81	10	0	200	200	180	50	10560.00	0	20	0	0	20	1	0	0	0	0	0	0	0	0	0
	30	82	5	90	200	200	180	50	10560.00	0	20	0	0	20	1	0	0	0	0	0	0	0	0	0
[100]	31	83	7	90	200	1200	100	30	180.00	0	20	0	0	20	1	0	0	0	0	0	0	0	0	0
	31	84	8	90	200	1900	100	30	180.00	0	20	0	0	20	1	0	0	0	0	0	0	0	0	0
[101]	32	85	16	90	340	1250	120	60	508.94	1	900	2	0	20	1	0	1	0	0	0	0	0	0	0
	32	86	11	90	340	1250	120	60	508.94	1	732	2	0	20	1	0	1	0	0	0	0	0	0	0
	32	87	13	90	340	1250	120	60	508.94	1	732	2	1	900	1000	2	1	0	0	0	0	0	0	0

Appendix B

Ti6Al4V fatigue BNN training database

Appendix C. Supplementary data

Supplementary data to this article can be found online at https://doi.org/10.1016/j.ijfatigue.2026.109481.

Data availability

The data that support the findings of this study are available from the corresponding author upon reasonable request.

References

[1] Gibson I, Rosen DW, Stucker B. Additive manufacturing technologies: rapid prototyping to direct digital manufacturing 2010. https://doi.org/10.1007/978-1-4419-1120-9.

[2] Yakout M, Elbestawi MA, Veldhuis SC. A review of metal additive manufacturing technologies. Solid State Phenom 2018. https://doi.org/10.4028/www.scientific.net/SSP.278.1.

[3] Frazier WE. Metal additive manufacturing: a review. J Mater Eng Perform 2014;23. https://doi.org/10.1007/s11665-014-0958-z.

[4] Plocher J, Panesar A. Review on design and structural optimisation in additive manufacturing: towards next-generation lightweight structures. Mater Des 2019;183. https://doi.org/10.1016/j.matdes.2019.108164.

[5] R Caivano, A Tridello, M Codegone, G Chiandussi, A new methodology for thermostructural topology optimization: analytical definition and validation, Proc Inst Mech Eng, Part L: J Mater: Design Appl 235 (2021). https://doi.org/10.1177/1464420720970246.

[6] C. Boursier Niutta, A. Tridello, G. Barletta, N. Gallo, A. Baroni, F. Berto, D.S. Paolino, Defect-driven topology optimization for fatigue design of additive manufacturing structures: application on a real industrial aerospace component, Eng Fail Anal 142 (2022). https://doi.org/10.1016/j.engfailanal.2022.106737.

[7] Benedetti M, du Plessis A, Ritchie RO, Dallago M, Razavi N, Berto F. Architected cellular materials: a review on their mechanical properties towards fatigue-tolerant design and fabrication. Mater Sci Eng R: Rep 2021;144. https://doi.org/10.1016/j.mser.2021.100606.

[8] Wu W, Hu W, Qian G, Liao H, Xu X, Berto F. Mechanical design and multifunctional applications of chiral mechanical metamaterials: a review. Mater Des 2019;180. https://doi.org/10.1016/j.matdes.2019.107950.

[9] Niutta CB, Ciardiello R, Tridello A. Experimental and numerical investigation of a lattice structure for energy absorption: application to the design of an automotive crash absorber. Polymers (Basel) 2022;14. https://doi.org/10.3390/polym14061116.

[10] Sanaei N, Fatemi A. Defects in additive manufactured metals and their effect on fatigue performance: a state-of-the-art review. Prog Mater Sci 2021;117:100724. https://doi.org/10.1016/J.PMATSCI.2020.100724.

[11] Ronchei C, Vantadori S, Carpinteri A. Fatigue lifetime assessment of AM metallic components according to a strain-based criterion. Int J Fatigue 2022;156:106674. https://doi.org/10.1016/J.IJFATIGUE.2021.106674.

[12] Leuders S, Lieneke T, Lammers S, Tröster T, Niendorf T. On the fatigue properties of metals manufactured by selective laser melting - the role of ductility. J Mater Res 2014;29. https://doi.org/10.1557/jmr.2014.157.

[13] Du L, Qian G, Zheng L, Hong Y. Influence of processing parameters of selective laser melting on high-cycle and very-high-cycle fatigue behaviour of Ti-6Al-4V. Fatigue Fract Eng Mater Struct 2021;44. https://doi.org/10.1111/ffe.13361.

[14] Tridello A, Fiocchi J, Biffi CA, Chiandussi G, Rossetto M, Tuissi A, et al. VHCF response of Gaussian SLM AlSi10Mg specimens: effect of a stress relief heat treatment. Int J Fatigue 2019;124. https://doi.org/10.1016/j.ijfatigue.2019.02.020.

[15] Tridello A, Fiocchi J, Biffi CA, Rossetto M, Tuissi A, Paolino DS. Size-effects affecting the fatigue response up to 109 cycles (VHCF) of SLM AlSi10Mg specimens produced in horizontal and vertical directions. Int J Fatigue 2022;160. https://doi.org/10.1016/j.ijfatigue.2022.106825.

[16] Yamashita Y, Murakami T, Mihara R, Okada M, Murakami Y. Defect analysis and fatigue design basis for Ni-based superalloy 718 manufactured by additive manufacturing. Procedia Struct Integrity 2017. https://doi.org/10.1016/j.prostr.2017.11.054.

[17] Moghtaderi SH, Jedi A, Ariffin AK, Thamburaja P. Application of machine learning in fracture analysis of edge crack semi-infinite elastic plate. Frattura Ed Integrita Strutturale 2024;18. https://doi.org/10.3221/IGF-ESIS.68.13.

[18] Azadi M, Matin M. Interpretation of fatigue lifetime prediction by machine learning modeling in piston aluminum alloys under different manufacturing and loading conditions. Frattura Ed Integrità Strutturale 2024;18. https://doi.org/10.3221/igf-esis.68.24.

[19] Beretta S, Romano S. A comparison of fatigue strength sensitivity to defects for materials manufactured by AM or traditional processes. Int J Fatigue 2017;94. https://doi.org/10.1016/j.ijfatigue.2016.06.020.

[20] Masuo H, Tanaka Y, Morokoshi S, Yagura H, Uchida T, Yamamoto Y, et al. Influence of defects, surface roughness and HIP on the fatigue strength of Ti-6Al-4V manufactured by additive manufacturing. Int J Fatigue 2018;117. https://doi.org/10.1016/j.ijfatigue.2018.07.020.

[21] Solberg K, Guan S, Razavi N, Welo T, Chan KC, Berto F. Fatigue of additively manufactured 316L stainless steel: the influence of porosity and surface roughness. Fatigue Fract Eng Mater Struct 2019;42. https://doi.org/10.1111/ffe.13077.

[22] Centola A, Tridello A, Ciampaglia A, Berto F, Paolino DS. Review on machine learning techniques for the assessment of the fatigue response of additively manufactured metal parts. Fatigue Fract Eng Mater Struct 2024. https://doi.org/10.1111/ffe.14326.

[23] Centola A, Ciampaglia A, Tridello A, Paolino DS. Machine learning methods to predict the fatigue life of selectively laser melted Ti6Al4V components. Fatigue Fract Eng Mater Struct 2023;46. https://doi.org/10.1111/ffe.14125.

[24] Tridello A, Ciampaglia A, Berto F, Paolino DS. Assessment of the critical defect in additive manufacturing components through machine learning algorithms. Appl Sci (Switzerland) 2023;13. https://doi.org/10.3390/app13074294.

[25] Maleki E, Bagherifard S, Guagliano M. Correlation of residual stress, hardness and surface roughness with crack initiation and fatigue strength of surface treated additive manufactured AlSi10Mg: experimental and machine learning approaches. J Mater Res Technol 2023;24:3265–83. https://doi.org/10.1016/J.JMRT.2023.03.193.

[26] Dang L, He X, Tang D, Li Y, Wang T. A fatigue life prediction approach for laser-directed energy deposition titanium alloys by using support vector regression based on pore-induced failures. Int J Fatigue 2022;159. https://doi.org/10.1016/j.ijfatigue.2022.106748.

[27] Horňas J, Běhal J, Homola P, Senck S, Holzleitner M, Godja N, et al. Modelling fatigue life prediction of additively manufactured Ti-6Al-4V samples using machine learning approach. Int J Fatigue 2023;169:107483. https://doi.org/10.1016/J.IJFATIGUE.2022.107483.

[28] Zhang M, Sun CN, Zhang X, Goh PC, Wei J, Hardacre D, et al. High cycle fatigue life prediction of laser additive manufactured stainless steel: a machine learning approach. Int J Fatigue 2019;128:105194. https://doi.org/10.1016/J.IJFATIGUE.2019.105194.

[29] Raissi M, Perdikaris P, Karniadakis GE. Physics-informed neural networks: a deep learning framework for solving forward and inverse problems involving nonlinear partial differential equations. J Comput Phys 2019;378:686–707. https://doi.org/10.1016/J.JCP.2018.10.045.

[30] Ciampaglia A, Tridello A, Paolino DS, Berto F. Data driven method for predicting the effect of process parameters on the fatigue response of additive manufactured AlSi10Mg parts. Int J Fatigue 2023;170:107500. https://doi.org/10.1016/J.IJFATIGUE.2023.107500.

[31] Ciampaglia A, Tridello A, Berto F, Paolino D. Data-driven method to assess the influence of process parameters on the fatigue response of additively manufactured Ti6Al4V. Procedia Struct Integrity 2023;47:56–69. https://doi.org/10.1016/j.prostr.2023.06.041.

[32] Murakami Y. Metal fatigue: effects of small defects and nonmetallic inclusions 2019. https://doi.org/10.1016/C2016-0-05272-5.

[33] Murakami Y, Masuo H, Tanaka Y, Nakatani M. Defect analysis for additively manufactured materials in fatigue from the viewpoint of quality control and statistics of extremes. Procedia Struct Integrity 2019;19:113–22. https://doi.org/10.1016/J.PROSTR.2019.12.014.

[34] Salvati E, Tognan A, Laurenti L, Pelegatti M, De Bona F. A defect-based physics-informed machine learning framework for fatigue finite life prediction in additive manufacturing. Mater Des 2022;222:111089. https://doi.org/10.1016/J.MATDES.2022.111089.

[35] Centola A, Ciampaglia A, Paolino DS, Tridello A. Probabilistic machine learning for preventing fatigue failures in additively manufactured SS316L. Eng Fail Anal 2025;168:109081. https://doi.org/10.1016/J.ENGFAILANAL.2024.109081.

[36] Chen J, Liu Y. Fatigue property prediction of additively manufactured Ti-6Al-4V using probabilistic physics-guided learning. Addit Manuf 2021;39:101876. https://doi.org/10.1016/J.ADDMA.2021.101876.

[37] Cutolo A, Lammens N, Vanden Boer K, Erdelyi H, Schulz M, Muralidharan GK, et al. Van Hooreweder, fatigue life prediction of a L-PBF component in Ti-6Al-4V using sample data, FE-based simulations and machine learning. Int J Fatigue 2023;167:107276. https://doi.org/10.1016/J.IJFATIGUE.2022.107276.

[38] C Blundell, J Cornebise, K Kavukcuoglu, D Wierstra, Weight uncertainty in neural networks, in: 32nd International Conference on Machine Learning, ICML 2015, 2015.

[39] Lee YL, Pan J, Hathaway R, Barkey M. Fatigue testing and analysis 2005. https://doi.org/10.1016/B978-0-7506-7719-6.X5000-3.

[40] Romano S, Abel A, Gumpinger J, Brandão AD, Beretta S. Quality control of AlSi10Mg produced by SLM: metallography versus CT scans for critical defect size assessment. Addit Manuf 2019;28:394–405. https://doi.org/10.1016/J.ADDMA.2019.05.017.

[41] du Plessis A, Yadroitsava I, Yadroitsev I. Effects of defects on mechanical properties in metal additive manufacturing: a review focusing on X-ray tomography insights. Mater Des 2020;187:108385. https://doi.org/10.1016/J.MATDES.2019.108385.

[42] Meng L, Zhang W, Quan D, Shi G, Tang L, Hou Y, et al. From topology optimization design to additive manufacturing: today's success and tomorrow's roadmap. Arch Comput Meth Eng 2020;27. https://doi.org/10.1007/s11831-019-09331-1.

[43] Boursier Niutta C, Tridello A, Paolino DS. Fatigue design of additive manufacturing components through topology optimization: comparison of

methodologies based on the defect distribution and on the stress gradient. Fatigue Fract Eng Mater Struct 2023;46. https://doi.org/10.1111/ffe.14082.
[44] Chen Y, Wang Q, Wang C, Gong P, Shi Y, Yu Y, et al. Topology optimization design and experimental research of a 3d-printed metal aerospace bracket considering fatigue performance. Appl Sci (Switzerland) 2021;11. https://doi.org/10.3390/app11156671.
[45] Cai S, Zhang W. Stress constrained topology optimization with free-form design domains. Comput Methods Appl Mech Eng 2015;289. https://doi.org/10.1016/j.cma.2015.02.012.
[46] Zhan Z, Li H. A novel approach based on the elastoplastic fatigue damage and machine learning models for life prediction of aerospace alloy parts fabricated by additive manufacturing. Int J Fatigue 2021;145. https://doi.org/10.1016/j.ijfatigue.2020.106089.
[47] Ciampaglia A, Santini A, Belingardi G. Design and analysis of automotive lightweight materials suspension based on finite element analysis. Proc Inst Mech Eng C J Mech Eng Sci 2021;235. https://doi.org/10.1177/0954406220947457.
[48] GE jet engine bracket challenge, (n.d.). https://grabcad.com/challenges/ge-jet-engine-bracket-challenge (accessed April 4, 2025).
[49] Günther J, Krewerth D, Lippmann T, Leuders S, Tröster T, Weidner A, et al. Fatigue life of additively manufactured Ti–6Al–4V in the very high cycle fatigue regime. Int J Fatigue 2017;94. https://doi.org/10.1016/j.ijfatigue.2016.05.018.
[50] Hu YN, Wu SC, Wu ZK, Zhong XL, Ahmed S, Karabal S, et al. A new approach to correlate the defect population with the fatigue life of selective laser melted Ti-6Al-4V alloy. Int J Fatigue 2020;136. https://doi.org/10.1016/j.ijfatigue.2020.105584.
[51] Le VD, Pessard E, Morel F, Edy F. Interpretation of the fatigue anisotropy of additively manufactured TA6V alloys via a fracture mechanics approach. Eng Fract Mech 2019;214. https://doi.org/10.1016/j.engfracmech.2019.03.048.
[52] Alegre JM, Díaz A, García R, Peral LB, Cuesta II. Effect of HIP post-processing at 850 °C/200 MPa in the fatigue behavior of Ti-6Al-4V alloy fabricated by selective laser melting. Int J Fatigue 2022;163:107097. https://doi.org/10.1016/J.IJFATIGUE.2022.107097.
[53] Soltani-Tehrani A, Habibnejad-Korayem M, Shao S, Haghshenas M, Shamsaei N. Ti-6Al-4V powder characteristics in laser powder bed fusion: the effect on tensile and fatigue behavior. Addit Manuf 2022;51:102584. https://doi.org/10.1016/J.ADDMA.2021.102584.
[54] Hu YN, Wu SC, Withers PJ, Zhang J, Bao HYX, Fu YN, et al. The effect of manufacturing defects on the fatigue life of selective laser melted Ti-6Al-4V structures. Mater Des 2020;192:108708. https://doi.org/10.1016/J.MATDES.2020.108708.
[55] Tridello A, Fiocchi J, Biffi CA, Chiandussi G, Rossetto M, Tuissi A, et al. VHCF response of heat-treated SLM Ti6Al4V Gaussian specimens with large loaded volume. Procedia Struct Integrity 2019. https://doi.org/10.1016/j.prostr.2019.08.171.
[56] Macallister N, Becker TH. Fatigue life estimation of additively manufactured Ti-6Al-4V: sensitivity, scatter and defect description in damage-tolerant models. Acta Mater 2022;237:118189. https://doi.org/10.1016/J.ACTAMAT.2022.118189.
[57] Wu L, Jiao Z, Yu H. Study on small crack growth behavior of laser powder bed fused Ti6Al4V alloy. Fatigue Fract Eng Mater Struct 2022;45. https://doi.org/10.1111/ffe.13725.
[58] Verma R, Kumar P, Jayaganthan R, Pathak H. Extended finite element simulation on tensile, fracture toughness and fatigue crack growth behaviour of additively manufactured Ti6Al4V alloy. Theor Appl Fract Mech 2022;117. https://doi.org/10.1016/j.tafmec.2021.103163.
[59] Walker KF, Liu Q, Brandt M. Evaluation of fatigue crack propagation behaviour in Ti-6Al-4V manufactured by selective laser melting. Int J Fatigue 2017;104:302–8. https://doi.org/10.1016/J.IJFATIGUE.2017.07.014.
[60] Bertolini R, Campagnolo A, Sorgato M, Ghiotti A, Bruschi S, Meneghetti G. Fatigue strength of LPBF Ti6Al4V machined under flood and cryogenic lubri-cooling conditions. Int J Fatigue 2022;162:106973. https://doi.org/10.1016/J.IJFATIGUE.2022.106973.
[61] Xu Z, Liu A, Wang X, Liu B, Guo M. Fatigue limit prediction model and fatigue crack growth mechanism for selective laser melting Ti6Al4V samples with inherent defects. Int J Fatigue 2021;143. https://doi.org/10.1016/j.ijfatigue.2020.106008.
[62] Sun C, Chi W, Wang W, Duan Y. Characteristic and mechanism of crack initiation and early growth of an additively manufactured Ti-6Al-4V in very high cycle fatigue regime. Int J Mech Sci 2021;205:106591. https://doi.org/10.1016/J.IJMECSCI.2021.106591.
[63] Spierings AB, Starr TL, Wegener K. Fatigue performance of additive manufactured metallic parts. Rapid Prototyp J 2013;19. https://doi.org/10.1108/13552541311302932.
[64] Shrestha R, Simsiriwong J, Shamsaei N. Fatigue behavior of additive manufactured 316L stainless steel parts: effects of layer orientation and surface roughness. Addit Manuf 2019;28. https://doi.org/10.1016/j.addma.2019.04.011.
[65] Stern F, Becker L, Cui C, Tenkamp J, Uhlenwinkel V, Steinbacher M, et al. Improving the defect tolerance of PBF-LB/M processed 316L steel by increasing the nitrogen content. Adv Eng Mater 2023;25. https://doi.org/10.1002/adem.202200751.
[66] Lai WJ, Ojha A, Li Z, Engler-Pinto C, Su X. Effect of residual stress on fatigue strength of 316L stainless steel produced by laser powder bed fusion process. Prog Addit Manuf 2021;6. https://doi.org/10.1007/s40964-021-00164-8.
[67] Kumar P, Jayaraj R, Suryawanshi J, Satwik UR, McKinnell J, Ramamurty U. Fatigue strength of additively manufactured 316L austenitic stainless steel. Acta Mater 2020;199. https://doi.org/10.1016/j.actamat.2020.08.033.
[68] Ponticelli GS, Panciroli R, Venettacci S, Tagliaferri F, Guarino S. Experimental investigation on the fatigue behavior of laser powder bed fused 316L stainless steel. CIRP J Manuf Sci Technol 2022;38. https://doi.org/10.1016/j.cirpj.2022.07.007.
[69] Shrestha R, Simsiriwong J, Shamsaei N. Fatigue behavior of additive manufactured 316L stainless steel under axial versus rotating-bending loading: synergistic effects of stress gradient, surface roughness, and volumetric defects. Int J Fatigue 2021;144. https://doi.org/10.1016/j.ijfatigue.2020.106063.
[70] Kotzem D, Kleszczynski S, Stern F, Elspaß A, Tenkamp J, Witt G, et al. Impact of single structural voids on fatigue properties of AISI 316L manufactured by laser powder bed fusion. Int J Fatigue 2021;148. https://doi.org/10.1016/j.ijfatigue.2021.106207.
[71] Liang X, Hor A, Robert C, Salem M, Lin F, Morel F. High cycle fatigue behavior of 316L steel fabricated by laser powder bed fusion: effects of surface defect and loading mode. Int J Fatigue 2022;160. https://doi.org/10.1016/j.ijfatigue.2022.106843.
[72] Zeng F, Yang Y, Qian G. Fatigue properties and S-N curve estimating of 316L stainless steel prepared by SLM. Int J Fatigue 2022;162. https://doi.org/10.1016/j.ijfatigue.2022.106946.
[73] Nafar Dastgerdi J, Jaberi O, Remes H. Influence of internal and surface defects on the fatigue performance of additively manufactured stainless steel 316L. Int J Fatigue 2022;163. https://doi.org/10.1016/j.ijfatigue.2022.107025.
[74] Yu C, Zhang P, Zhang Z, Liu W. Microstructure and fatigue behavior of laser-powder bed fusion austenitic stainless steel. J Mater Sci Technol 2020;46. https://doi.org/10.1016/j.jmst.2019.08.047.
[75] Cui L, Deng D, Jiang F, Peng RL, Xin T, Mousavian RT, et al. Superior low cycle fatigue property from cell structures in additively manufactured 316L stainless steel. J Mater Sci Technol 2022;111. https://doi.org/10.1016/j.jmst.2021.10.006.
[76] Malekipour K, Mashayekhi M, Badrossamay M. Meso-scale damage mechanics modeling for high cycle fatigue behavior of additively manufactured components. Mech Mater 2021;160. https://doi.org/10.1016/j.mechmat.2021.103951.
[77] Uhlmann E, Fleck C, Gerlitzky G, Faltin F. Dynamical fatigue behavior of additive manufactured products for a fundamental life cycle approach. Procedia CIRP 2017. https://doi.org/10.1016/j.procir.2016.11.138.
[78] Voloskov B, Evlashin S, Dagesyan S, Abaimov S, Akhatov I, Sergeichev I. Very high cycle fatigue behavior of additively manufactured 316L stainless steel. Materials 2020;13. https://doi.org/10.3390/ma13153293.
[79] Zhao X, Li S, Zhang M, Liu Y, Sercombe TB, Wang S, et al. Comparison of the microstructures and mechanical properties of Ti–6Al–4V fabricated by selective laser melting and electron beam melting. Mater Des 2016;95:21–31. https://doi.org/10.1016/J.MATDES.2015.12.135.
[80] Fousová M, Vojtěch D, Doubrava K, Daniel M, Lin CF. Influence of inherent surface and internal defects on mechanical properties of additively manufactured Ti6Al4V alloy: comparison between selective laser melting and electron beam melting. Materials 2018;11. https://doi.org/10.3390/ma11040537.
[81] Jiang Q, Li S, Zhou C, Zhang B, Zhang Y. Effects of laser shock peening on the ultra-high cycle fatigue performance of additively manufactured Ti6Al4V alloy. Opt Laser Technol 2021;144:107391. https://doi.org/10.1016/J.OPTLASTEC.2021.107391.
[82] Eric W, Claus E, Shafaqat S, Frank W. High cycle fatigue (HCF) performance of Ti-6Al-4V alloy processed by selective laser melting. Adv Mat Res 2013. https://doi.org/10.4028/www.scientific.net/AMR.816-817.134.
[83] Gong H, Rafi K, Gu H, Janaki Ram GD, Starr T, Stucker B. Influence of defects on mechanical properties of Ti–6Al–4 V components produced by selective laser melting and electron beam melting. Mater Des 2015;86:545–54. https://doi.org/10.1016/J.MATDES.2015.07.147.
[84] Mertova K, Dzugan J, Roudnicka M. Fatigue properties of SLM-produced Ti6Al4V with various post-processing processes. IOP Conf Ser: Mater Sci Eng 2018. https://doi.org/10.1088/1757-899X/461/1/012052.
[85] Yan X, Yin S, Chen C, Jenkins R, Lupoi R, Bolot R, et al. Fatigue strength improvement of selective laser melted ti6al4v using ultrasonic surface mechanical attrition. Mater Res Lett 2019;7. https://doi.org/10.1080/21663831.2019.1609110.
[86] Kumar P, Ramamurty U. High cycle fatigue in selective laser melted Ti-6Al-4V. Acta Mater 2020;194. https://doi.org/10.1016/j.actamat.2020.05.041.
[87] Xin R, Lan L, Bai C, Gao S, He B, Wang J. Fatigue properties of selective laser melted Ti-6Al-4V alloy subjected to laser shock processing. J Mater Sci 2022;57. https://doi.org/10.1007/s10853-022-07019-9.
[88] Dietrich K, Diller J, Dubiez-Le Goff S, Bauer D, Forêt P, Witt G. The influence of oxygen on the chemical composition and mechanical properties of Ti-6Al-4V during laser powder bed fusion (L-PBF). Addit Manuf 2020;32:100980. https://doi.org/10.1016/J.ADDMA.2019.100980.
[89] Lee S, Rasoolian B, Silva DF, Pegues JW, Shamsaei N. Surface roughness parameter and modeling for fatigue behavior of additive manufactured parts: a non-destructive data-driven approach. Addit Manuf 2021;46:102094. https://doi.org/10.1016/J.ADDMA.2021.102094.
[90] Asherloo M, Wu Z, Heim M, Nelson D, Paliwal M, Rollett AD, et al. Fatigue performance of laser powder bed fusion hydride-dehydride Ti-6Al-4V powder. Addit Manuf 2022;59:103117. https://doi.org/10.1016/J.ADDMA.2022.103117.
[91] Bhandari L, Gaur V. On study of process induced defects-based fatigue performance of additively manufactured Ti6Al4V alloy. Addit Manuf 2022;60:103227. https://doi.org/10.1016/J.ADDMA.2022.103227.

[92] Gillham B, Yankin A, McNamara F, Tomonto C, Taylor D, Lupoi R. Application of the theory of critical distances to predict the effect of induced and process inherent defects for SLM Ti-6Al-4V in high cycle fatigue. CIRP Ann 2021;70:171–4. https://doi.org/10.1016/J.CIRP.2021.03.004.

[93] Ghiotti A, Bertolini R, Sorgato M, Campagnolo A, Savio E, Bruschi S. Ti6Al4V titanium alloy fatigue strength after AM- and machining-based process chains. CIRP Ann 2022;71:461–4. https://doi.org/10.1016/J.CIRP.2022.04.021.

[94] Gupta A, Bennett CJ, Sun W. High cycle fatigue performance evaluation of a laser powder bed fusion manufactured Ti-6Al-4V bracket for aero-engine applications. Eng Fail Anal 2022;140:106494. https://doi.org/10.1016/J.ENGFAILANAL.2022.106494.

[95] Yu H, Li F, Wang Z, Zeng X. Fatigue performances of selective laser melted Ti-6Al-4V alloy: Influence of surface finishing, hot isostatic pressing and heat treatments. Int J Fatigue 2019;120:175–83. https://doi.org/10.1016/J.IJFATIGUE.2018.11.019.

[96] Xu Z, Liu A, Wang X, Liu B, Guo M. Fatigue limit prediction model and fatigue crack growth mechanism for selective laser melting Ti6Al4V samples with inherent defects. Int J Fatigue 2021;143:106008. https://doi.org/10.1016/J.IJFATIGUE.2020.106008.

[97] Yan X, Yin S, Chen C, Huang C, Bolot R, Lupoi R, et al. Effect of heat treatment on the phase transformation and mechanical properties of Ti6Al4V fabricated by selective laser melting. J Alloy Compd 2018;764:1056–71. https://doi.org/10.1016/J.JALLCOM.2018.06.076.

[98] Chang K, Liang E, Huang W, Zhang X, Chen Y, Dong J, et al. Microstructural feature and mechanical property in different building directions of additive manufactured Ti6Al4V alloy. Mater Lett 2020;267:127516. https://doi.org/10.1016/J.MATLET.2020.127516.

[99] Edwards P, Ramulu M. Fatigue performance evaluation of selective laser melted Ti–6Al–4V. Mater Sci Eng A 2014;598:327–37. https://doi.org/10.1016/J.MSEA.2014.01.041.

[100] Segurajauregi U, Álvarez-Vázquez A, Muñiz-Calvente M, Urresti Í, Naveiras H. Fatigue assessment of selective laser melted ti-6al-4v: influence of speed manufacturing and porosity. Metals (Basel) 2021;11. https://doi.org/10.3390/met11071022.

[101] Jimenez EH, Kreitcberg A, Moquin E, Brailovski V. Influence of post-processing conditions on the microstructure, static, and fatigue resistance of laser powder bed fused Ti-6Al-4V components. J Manuf Mater Process 2022;6. https://doi.org/10.3390/jmmp6040085.